Fall 2009

Numerical modeling and analysis of complex electromagnetic structures, including those containing ferrites

Andrea Orlando

Department:

NUMERICAL MODELING AND ANALYSIS OF COMPLEX ELECTROMAGNETIC STRUCTURES, INCLUDING THOSE CONTAINING FERRITES

by

ANDREA ORLANDO

A THESIS

Presented to the Faculty of the Graduate School of the

MISSOURI UNIVERSITY OF SCIENCE AND TECHNOLOGY

In Partial Fulfillment of the Requirements for the Degree

MASTER OF SCIENCE IN ELECTRICAL ENGINEERING

2009

Approved by

Marina Y. Koledintseva, Advisor
James L. Drewniak
Daryl G. Beetner

ABSTRACT

Application of fast switching amplifiers in power converters, and especially in power inverters, causes unwanted radiated emission, which is a consequence of common mode (CM) currents arising in feed wire bundles. Ferrite chokes are commonly used to suppress those CM currents by increasing the CM impedance of circuits without affecting the differential mode currents, which is important for undisturbed operation of the converters or inverters. Their effective impedance is the main design concern, and it is determined by the material intrinsic properties (permeability, permittivity) and geometry.

The goal of this work is to analytically correlate the geometrical and material properties (permittivity and magnetic permeability) of a ferrite choke under test conditions with its extracted equivalent circuit parameters (resistance, inductance and capacitance) and complex impedance of the ferrite choke on a wire bundle. The identification of those above mentioned equivalent circuit parameters can help to identify the best combination of dimension-material properties to maximize the efficiency of ferrites for suppressing CM currents.

ACKNOWLEDGMENTS

I would like to express my sincere gratitude and deep appreciation to my advisor, Dr. Marina Y. Koledintseva, for his invaluable support of my research work and her guidance throughout my graduate work.

Dr. James L. Drewniak and Dr. Daryl Beetner were always willing to sacrifice their time to answer my questions, and for that I am grateful. I thank them for initiating insightful technical discussions and for guiding me in the completion of my dissertation. Special thanks are due to my former professor Antonio Orlandi, for all his assistance and particularly for his help in bringing me to the United States.

I would like to express my deepest thanks to my parents, Pasquale and Rosanna, and my brother, Michele, for their unwavering support and unconditional encouragement throughout my education; I am glad to dedicate this work to them for their effort to make my dreams of higher education a reality despite the great effort it cost them. I would also like to extend my warm appreciation to all my family members for their unrelenting support and encouragement. I am profoundly grateful to Francesco, Matteo, Mimma, Hemant, Amendra, Evgeniy, Argha, Jing, Emanuela, Marianna, and Antonio for supporting me morally and for helping in the difficult moments. Additionally, I am grateful to all the members of the Electromagnetic Compatibility Laboratory at Missouri University of Science and Technology for helping me to become technically proficient. Finally, I thank God Almighty; His benediction made everything possible.

TABLE OF CONTENTS

Page

LIST OF ILLUSTRATIONS

Page

LIST OF TABLES

Page

NOMENCLATURE

Symbol	Description
α	Attenuation Constant (Real Part of Propagation Constant)
β	Phase Constant (Imaginary Part of Propagation Constant or $\omega\sqrt{\mu \cdot \varepsilon}$)
γ	Propagation Constant ($\gamma = \sqrt{j\omega\mu(\sigma + j\omega\varepsilon)} = \alpha + j\beta$)
ε	Electric Permettivity [F/m]
μ	Magnetic Permeability [H/m]
σ	Electrical Conductivity [S/m]
η_0	Intrinsic Impedance in Free Space ($Z_0 = \sqrt{\frac{\mu_0}{\varepsilon_0}}$)
η	Intrinsic Impedance of the Shield ($Z_m = \sqrt{\frac{j\omega\mu}{\sigma + j\omega\varepsilon}}$)
δ	Skin Depth for the Barrier Material ($\delta = \frac{1}{\sqrt{\pi f \mu \sigma}}$)
B	Magnetization Field [T]
H	Magnetization Field [A/m]
E	Electric Field [V/m]
D	Electric Displacement Field [C/m^2]
L	Inductance [H]
C	Capacitance [F]
R	Resistance [Ω]
G	Conductance [S]
γ'	Gyromagnetic Factor (γ/(2π) = 3 [MHz/Oe])

1. INTRODUCTION

Ferromagnetic and ferrite materials are widely used in electrical and electronic engineering. These materials can have pronounced magnetic properties; including high permeability due to the internal (spin) magnetic field of the electrons of magnetic atoms. The force responsible for the alignment of the electron spins occurs in only five elements: Iron (Fe), Nickel (Ni), Cobalt (Co), Dysprosium (Dy), and Gadolinium (Gd). Inside crystals of these materials there are spontaneously magnetized areas 10^{-2} to 10^{-4} cm; these regions are called domains. Every domain is a small permanent magnet. The main difference between ferromagnetic materials and ferrites is that ferromagnetic materials are typically magnetic metals with substantial electric conductivity, whereas ferrites are ferrimagnetic materials with negligible conductivity but comparatively high relative permittivity (~8 to 20).

Static magnetic properties depend on the chemical contents of a ferromagnetic or ferrite material, as well as on sintering conditions. Magnetic materials may be soft or hard, depending on the shape of their hysteresis curves. A wide hysteresis curve is characteristic of hard magnets, whereas a narrow hysteresis curve is observed in soft ferrites (Figure 1.1). Hard magnetic materials are typically used for permanent magnets; soft magnetic materials can be applied to the design of memory, switching devices, or noise suppressors. Noise suppressors are important for solving problems of electromagnetic compatibility and immunity because they eliminate unwanted electromagnetic radiations or coupling paths.

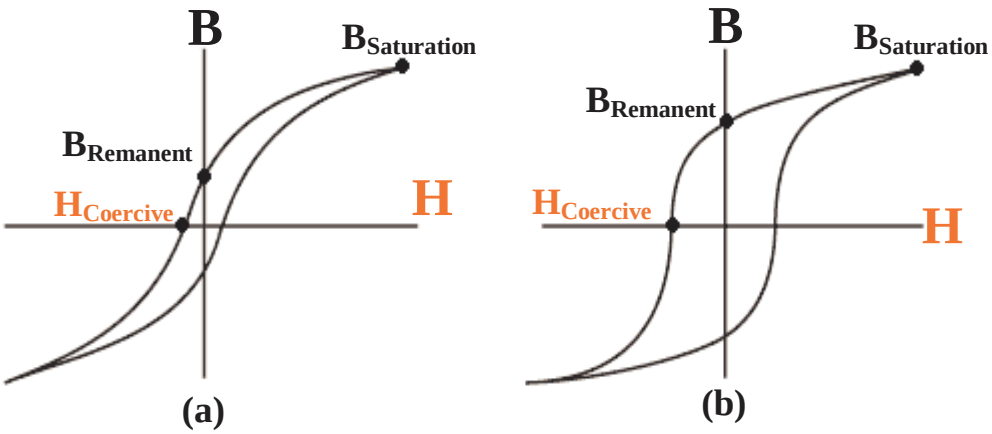

Figure 1.1. Magnetization curves for (a) soft and (b) hard ferrites/ferromagnets.

There are various ways to suppress unwanted electromagnetic interference:

- reduce emission at the noise source;
- terminate, divert, or make inefficient the existing coupling path;
- reduce susceptibility of circuit elements that could be affected by interference.

Figure 1.2 shows two main applications of ferrite and ferromagnetic materials, shielding and common-mode (CM) suppressors.

Due to their high permeability and conductivity, ferromagnetic conducting materials are widely used to shield against magnetostatic and electromagnetic fields. Attenuation in ferromagnetic shields is known to be proportional both to permeability and conductivity owing to the skin effect. However, the presence of eddy currents in walls or enclosures is not always desirable. Besides, shielding against magnetostatic and very low-frequency magnetic fields requires completely closed ferromagnetic surfaces, which are

not always practically possible. If there are slots or seams on an enclosure, and surface currents cross them, these slots or seams may become a part of unintentional antennas, providing undesired emissions and worsening EMC/EMI situation.

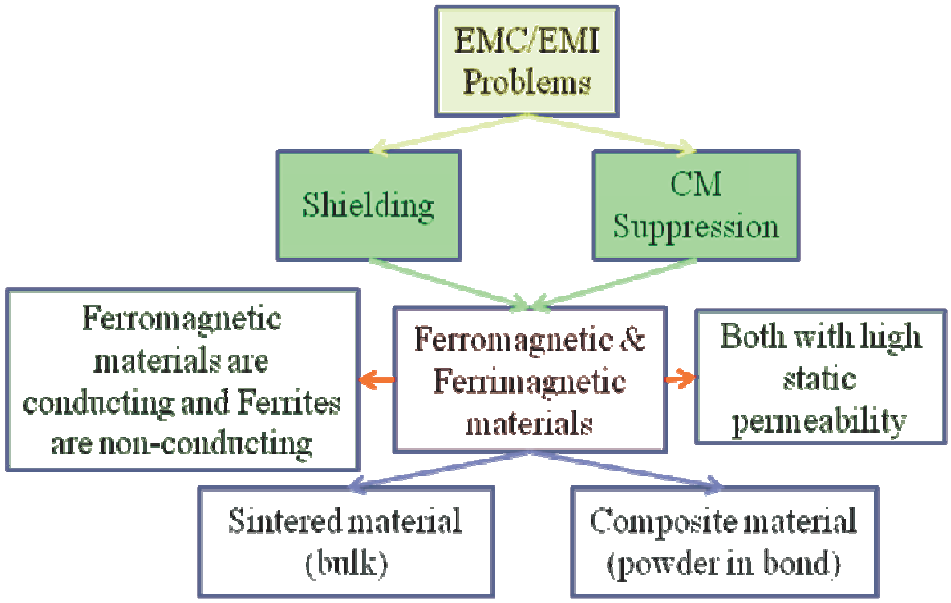

Figure 1.2. Main EMC/EMI applications of magnetic materials.

Nonconducting sintered ferrite tiles are widely used on the walls of anechoic chambers, shielded rooms, or enclosures for large electronic equipment or systems. They typically have high static permeability (on the order of a few thousand or even higher), but they are used at comparatively low frequencies (in MHz region at most), where permeability values are still high. The effectiveness of these tiles drops drastically beyond a cutoff frequency, according to Snoek's law [1]:

$$(\mu_s - 1) \cdot f_r = \frac{2}{3} \cdot \gamma' \cdot 4\pi M_s \quad (1)$$

where $4\pi M_s$ (expressed in Gauss) is the saturation magnetization, $\gamma' = 2.8$ MHz/Oe is the gyromagnetic ratio (in SI system, $\gamma' = 1.76 \cdot 10^{11}$ C/kg), f_r is the cut-off frequency, and μ_s is the static permeability. Snoek's law is useful for estimating the microwave performance of magnetic materials. Therefore, f_r may be considered the permeability cut-off frequency, and μ_s is an estimation of the permeability within the operating frequency band (below cut-off). Equation (1) relates the product of μ_s and f_r to the saturation magnetization of the material. Within the limits established by Snoek's law, μ_s and f_r may often be varied within a wide range by technological means.

Bulk-sintered soft-ferrite spinel materials, e.g., Manganese-Zinc or Nickel-Zinc ferrites, are also employed in chokes with windings, or in sleeves that can be used around wires or cables to reduce CM currents. However, small ferrite beads are also used as inductance elements or filters on printed circuit boards.

Manganese-Zinc ferrites have higher initial permeability than Nickel-Zinc ferrites, but their permeability decreases faster with respect to frequency. Therefore, a ferrite core with higher initial permeability is not always the best solution because, in the range of radiated emissions (30-MHz to 40-GHz), the core with lower initial permeability (Nickel-Zinc) may better suppress the spectral components of currents in the specified frequency range. Thus, the choice of the core depends on the frequency components to be suppressed (related to conducted or radiated emissions). Figure 1.3 compares the

permeability of Manganese-Zinc and Nickel-Zinc ferrites [2]. It demonstrates clearly that in the frequency range from kHz to MHz Nickel-Zinc ferrites are better than Manganese-Zinc ferrites.

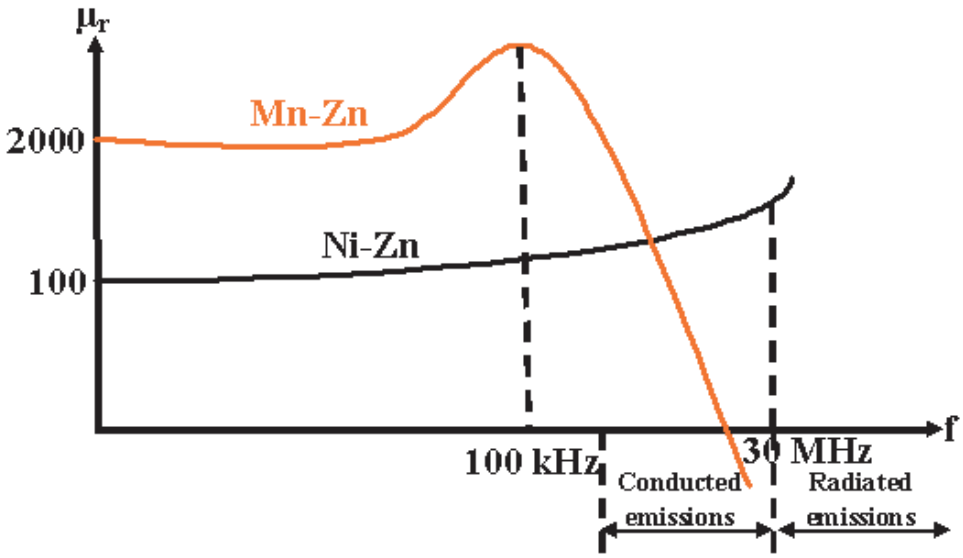

Figure 1.3. Manganese-Zinc versus Nickel-Zinc permeabilities.

Figure 1.4 shows the typical behavior of relative static permeability as a function of temperature at 100 kHz. It indicates that a drastic drop in static permeability identifies the achievement of the Curie temperature related to the particular ferrite under analysis.

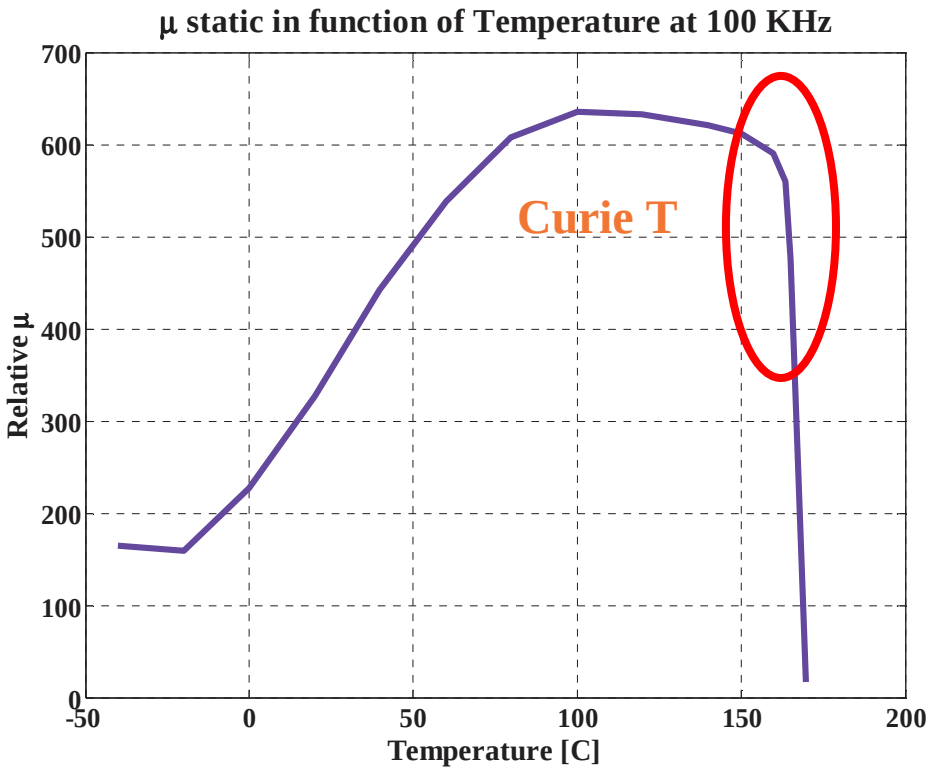

Figure 1.4. Static permeability as a function of temperature [these data have been provided by Laird Technologies].

Figure 1.5 shows the variation of relative static permeability as a function of the applied magnetization field, and it demonstrates how saturation affects the material properties of ferrites.

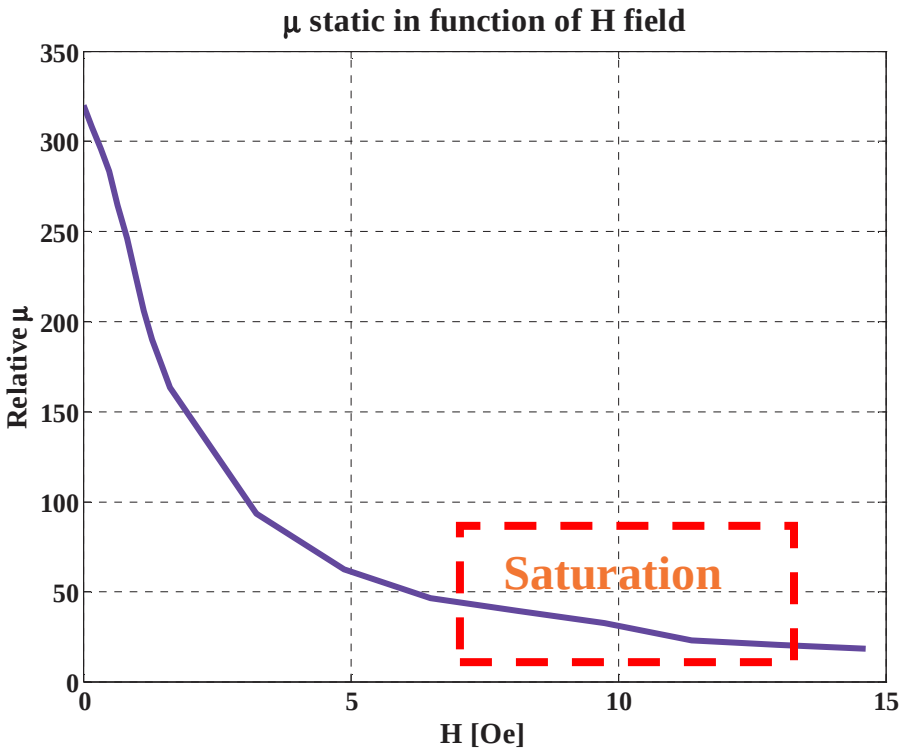

Figure 1.5. Static permeability variation as a function of applied magnetization field [these data have been provided by Laird Technologies].

Along with sintered materials, composite materials containing ferrite or ferromagnetic powders as fillers in a dielectric (polymer) base are now widely used for various EMC/EMI applications. Compared to sintered bulk ceramic ferrites, they have a lower density and weight. They are also sturdy, flexible, and easily cut or shaped by molding, so that comparatively thin sheets or layers may be formed from them. Composites containing ferrite or ferromagnetic inclusions can be used as electromagnetic wave absorbers (EMWA) or noise suppressing sheets (NSS). Currently, the interest of the electronic industry to such composite materials has increased. The attention they are receiving is related to the increased noise exposure inside high-speed digital designs due

to the trends toward microminiaturization and ever higher operation frequencies. The main advantage of polymer-based ferrite-containing composites is that frequency responses of complex permeability and permittivity can be synthesized according to practical requirements. The frequency characteristics of these composite materials makes them flexible so that they can be shaped as desired by varying the composite filler types, the size and concentration of inclusions and the morphology of mixtures through the alignment of inclusion particles.

2. CM CURRENT SUPPRESSOR

A common-mode suppressor can be identified by ferrite beads or by ferrite chokes. Definitions of common mode and differential mode currents are given in the appendix.

A ferrite bead with a ferrite material surrounding a wire resembles a resistor. Figure 2.1 shows its circuit schematic as a connected series of resistance and inductance [2]. The current that goes through the wire creates magnetic flux in the circumferential direction, and this flux produces an internal inductance $L_{bead} = \mu_0 \mu_r k$, where k is the geometry-dependent coefficient.

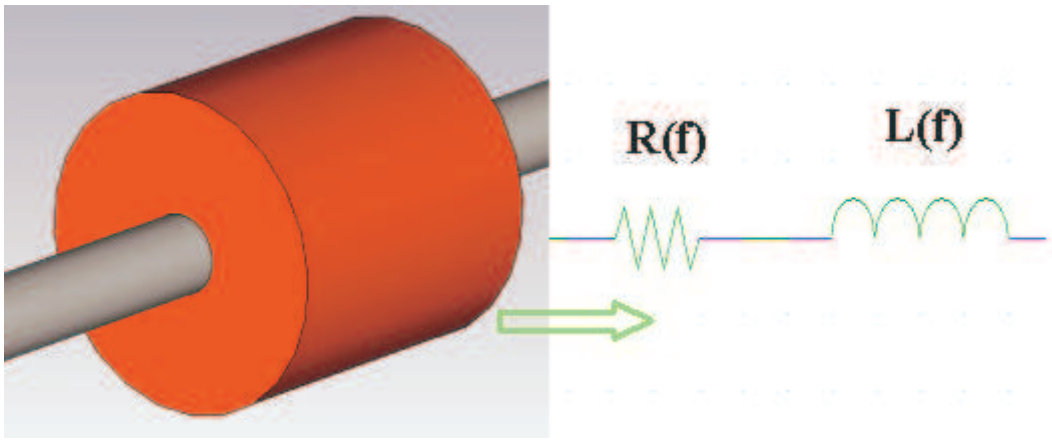

Figure 2.1. Example of ferrite bead and relative equivalent circuit.

Ferrite beads are typically used as EMI-noise suppression filters for frequencies up to 1 GHz [3]. The impedance of ferrite beads is on the order of 100 ohm at frequencies above 100 MHz, as shown in Figure 2.2 [4].

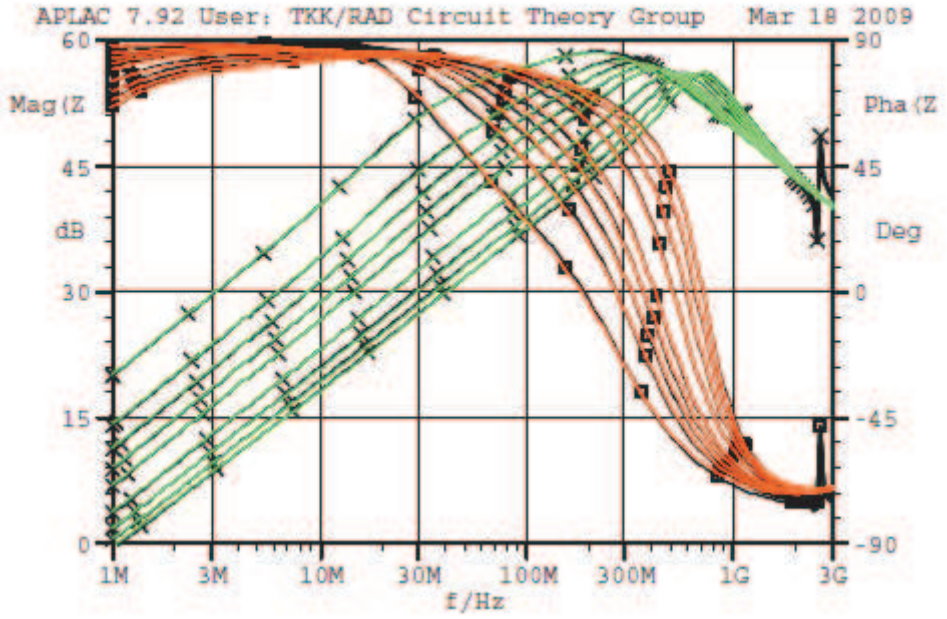

Figure 2.2. Measured impedances for ferrite beads.

Common-mode chokes are also used to suppress, reduce, or dissipate CM currents. The higher the CM impedance, the more effective the suppression of CM currents is. In Figure 2.3, a pair of wires carrying current is wound around the ferromagnetic core [2]. If the windings are symmetric and the flux remains in the core, the differential mode (DM) current is not affected by impedance associated with the choke. This case is ideal to avoid reduction of DM or functional currents in devices. In DM currents, for example, the signals passing from the source to the receiver within a device should not be affected by the choke. At the same time, these DM currents should not cause any variations in the choke performance, e.g., by saturating the ferrite material, or causing its parameter degradation by heating. The effectiveness of chokes is associated with the equality of the

mutual and self-inductances. High permeability which concentrates the flux in the core and symmetric winding ensure the effectiveness of chokes.

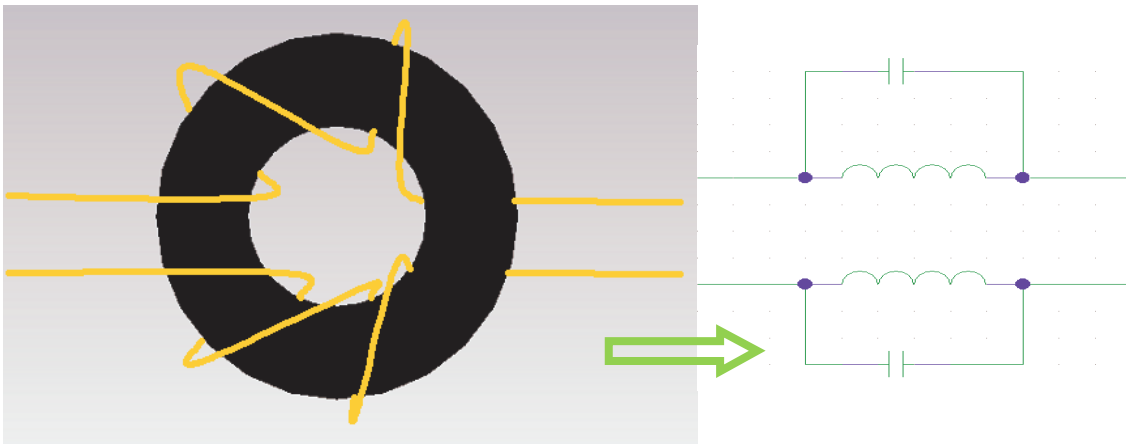

Figure 2.3. Winding example in a CM choke.

Figure 2.4 shows the ferrite choke studied in this work. This was a Manganese-Zinc ferrite choke developed and provided by Laird Technologies. The frequency characteristics of its permeability and permittivity are addressed in Section 2.1. This ferrite choke is intended to be used in an automotive three-phase power supply (inverter) used to obtain alternating (shown in Figure 2.5) currents (AC) from the direct current (DC) to feed a motor through a bundle of three wires. In this system, CM currents are produced by a switching power supply, and they may be a source of unwanted electromagnetic emission since the wire may become an unintentional antenna and affect susceptible circuits placed close to it. In this particular case, this work proposes that the ferrite choke with a clamp to be put around a bundle of wires in order to remove CM currents flowing from the power supply to the load.

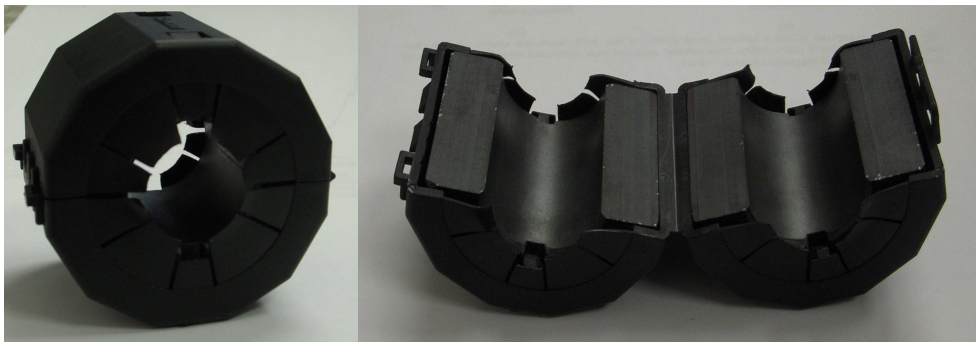

Figure 2.4. Ferrite choke under analysis.

Placing this ferrite as close as possible to the source of the emission (inverter) will reduce the unwanted conducted and radiated emissions by increasing the CM impedance without affecting the DM impedance. Figure 2.6 shows the wire bundle geometry and identifies the place where the ferrite choke is placed.

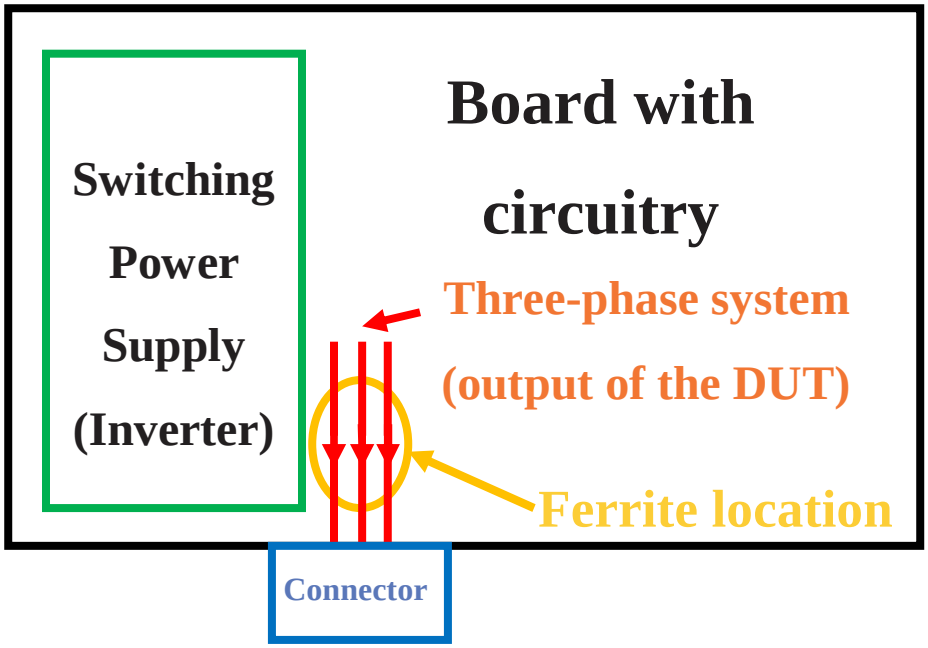

Figure 2.5. Representation of real EMI/EMC problem.

The objective of this work was to derive an equivalent lumped-element circuit model for the ferrite choke on the wire based on the geometry of the choke and of the wire as well as on the material properties of the ferrite. This goal required simplified numerical and physical (laboratory) models to represent the problem and permit extraction of the parameters of this equivalent circuit from both simulations and measurements. This model is discussed in Section 2.3. The abovementioned extraction is done by analyzing real and imaginary parts of input impedance of the circuit containing the ferrite choke. The input impedance Z_{in} must first be measured or simulated in an adequately detailed numerical model. It must then be correlated with the extracted RLC equivalent lumped-element circuit parameters of a ferrite choke. These steps represent a problem of interest not only for this particular case, but for any ferrite choke on a wire.

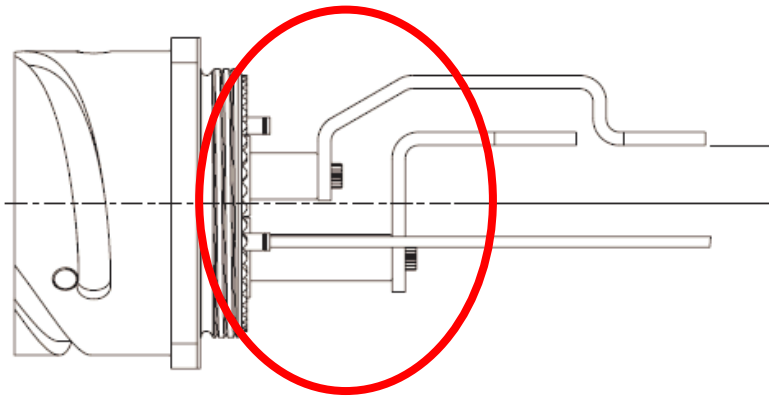

Figure 2.6. Ferrite location and wire shape.

2.1. MODELING MATERIAL PROPERTIES IN CST

Numerical modeling of ferrite chokes in a wide frequency range requires knowledge of complex constitutive electromagnetic properties of ferrites. From an

electromagnetic point of view, ferrites are frequency-dispersive magnetodielectric materials characterized by complex relative permeability:

$$\mu_r(\omega) = \mu'_r(\omega) - j \cdot \mu''_r(\omega) \tag{2}$$

and permittivity:

$$\varepsilon_r(\omega) = \varepsilon'_r(\omega) - j \cdot \varepsilon''_r(\omega). \tag{3}$$

The real parts of permeability $\mu_r(\omega)$ and permittivity $\varepsilon_r(\omega)$ are related to the stored magnetic and electric energy, respectively stored within the material. Real parts of $\mu_r(\omega)$ and $\varepsilon_r(\omega)$ are also associated with the phase velocity of the electromagnetic waves propagating within the medium. The corresponding imaginary parts are associated with the dissipation of magnetic and electric energy in the material and loss experienced by propagating electromagnetic waves.

Typically ferrites are very good insulators. Their DC conductivity is on the order of 10^{-13} to 10^{-14} S/m, and their static permittivity is on the order of ~10 to 20. Dielectric properties of ferrites depend on their chemical composition, sintering type, crystallographic structure, and grain morphology [5]. The corresponding relaxation occurs due to polarization loss. Complex permittivity of a ferrite can be described by the Debye frequency dependence suitable for dielectrics with permanent electric dipole moments:

$$\varepsilon_r(\omega) = \varepsilon_\infty + \frac{\varepsilon_s - \varepsilon_\infty}{1 + j\omega\tau_e} \tag{4}$$

where τ_e is the Debye relaxation time, related to the relaxation frequency f_e as

$$\tau_e = \frac{1}{2\pi f_e} \quad . \tag{5}$$

In equation (4), ε_s and ε_∞ indicate the static permittivity and so-called optical (or high frequency limit) permittivity, respectively. The imaginary component of complex permittivity defined as equation (4) is positive for all frequencies, and it has its maximum at the relaxation frequency (5). Figure 2.7 shows the Debye dispersive curves, with f_{rel} corresponding either to the dielectric relaxation frequency f_e or to the magnetic relaxation frequency f_m.

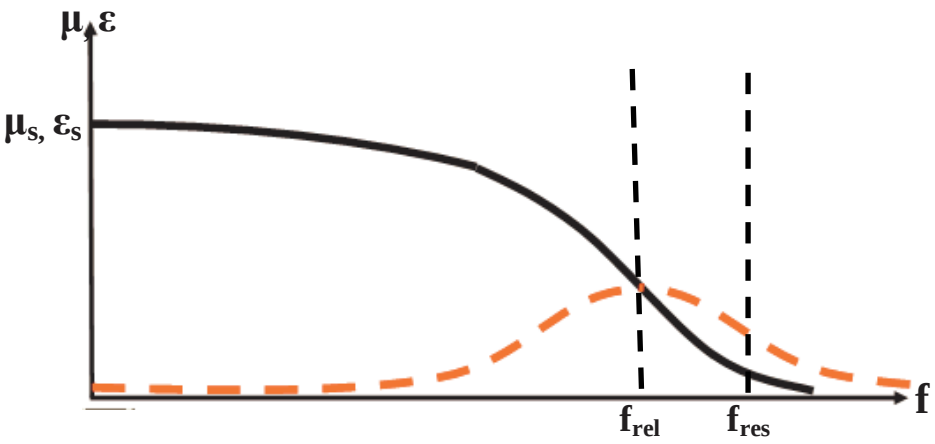

Figure 2.7. Debye dispersive curves.

Complex permeability of soft ferrites, like Nickel-Zinc or Manganese-Zinc, can also be represented using the Debye frequency dependence:

$$\tilde{\mu}(\omega) = \mu_\infty + \frac{\mu_s - \mu_\infty}{1 + j\omega\tau_m} = 1 + \frac{\mu_s - 1}{1 + j\omega\tau_m} \tag{6}$$

with the magnetic relaxation constant

$$\tau_m = \frac{1}{2\pi f_m} \tag{7}$$

where μ_s is the static permeability of the ferrite. Hence, the ferrite can be considered as the "double-Debye material" (DDM).

Material properties (permittivity and permeability) may also be represented by multiterm Debye models. Such representations permit reasonably accurate analytical approximation of the measured effective material properties. For this work, measurement of the complex permittivity and permeability of a ferrite material (in particular, Manganese-Zinc) was based on the methodology described in [6]. Measurements of complex permittivity and permeability require an input impedance Z_{in} of a specially-made silver-coated toroidal ferrite sample obtained by using either a vector network analyzer (VNA) or an impedance analyzer (IA). Measurements obtained with an IA are cheaper and simpler, but in a lower frequency range than those obtained by using a VNA. The internal and external cylindrical surfaces of the sample were coated with silver to form a

coaxial line, and the end of the sample was either “shorted” (i.e., coated with silver) or “opened” (without coating). The input impedances were then measured in “short” and “open” regimes of this coaxial line section, and the complex characteristic impedance of the sample was calculated as

$$Z_w = \sqrt{Z_{short} \cdot Z_{open}} \,. \tag{8}$$

Next, the frequency dependent complex permittivity and permeability are calculated using the coaxial transmission line theory, as described in [6]. A curve-fitting procedure based on a robust optimization genetic algorithm (GA) technique [7] was adopted to extract the parameters of the ferrite as a DDM over a wideband frequency range. A DDM is defined as a material whose permittivity and permeability can be represented as sums of Debye-like terms [8].

Figures 2.8 and 2.9 show the Debye material properties for the bulk Manganese-Zinc ferrite used in the choke, as well as for the bulk Nickel Zinc ferrite. In this particular case, two Debye terms are used to approximate dielectric properties, and two Debye terms were used to describe magnetic properties. The full-wave numerical electromagnetic tool CST Microwave Studio used here to model the coated sample performed an internal Debye approximation of the loaded material properties as functions of frequency. The number of Debye terms was limited by the capability of the software (CST Microwave Studio-2009), which cannot deal with more than two Debye terms each for permittivity and permeability. Two terms were sufficient for the frequency range involved here (below 1 GHz); however, for higher frequency approximations (tens of GHz) more Debye terms

would be needed. Figures 2.8 and 2.9 indicate that relaxation frequencies for magnetic and electric properties were different, which was to be expected since permittivity and permeability are two quite different and almost unrelated physical properties.

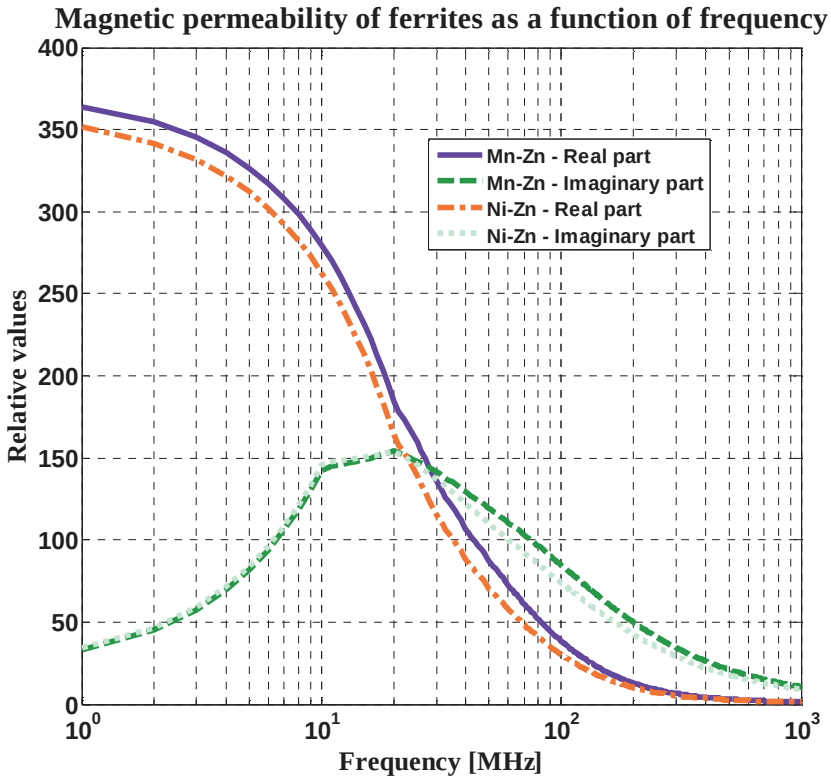

Figure 2.8. Permeability of Manganese-Zinc and Nickel-Zinc ferrites as a function of frequency [these data have been provided by Laird Technologies].

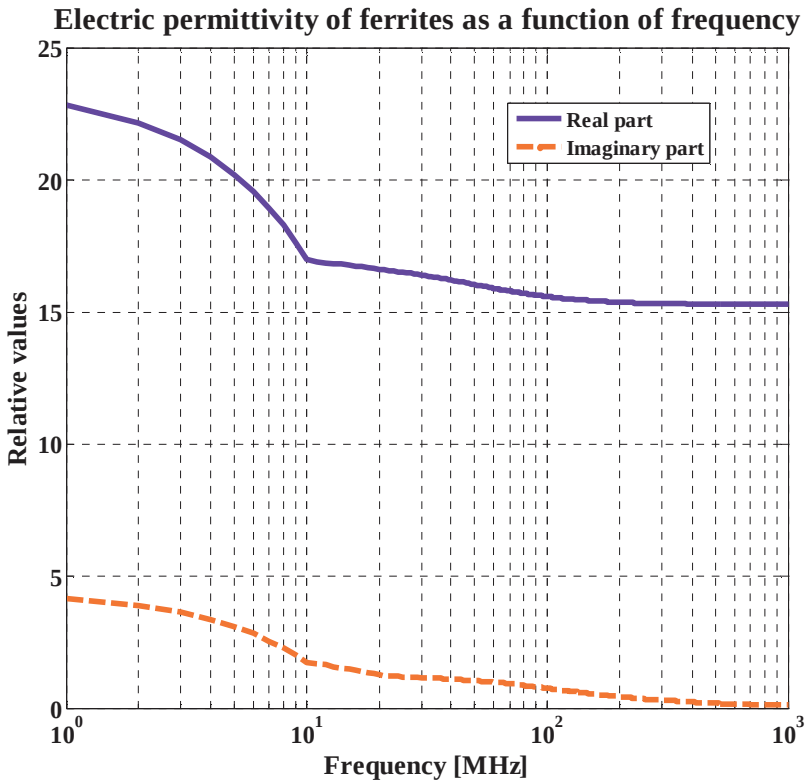

Figure 2.9. Permittivity of Manganese-Zinc and Nickel-Zinc ferrites as a function of frequency [these data have been provided by Laird Technologies].

Figures 2.8 and 2.9 display frequency dependencies for the permeability and permittivity of both Manganese-Zinc and Nickel-Zinc bulk ferrites. Permittivities are the same for the two materials. In practice, however, the Manganese-Zinc ferrite choke had two gaps because it was comprised of two ferrite parts clamped together around the wire. Although this gap was extremely narrow compared to the size of the choke, its presence substantially affected the magnetic properties of the choke. Nonetheless, it did not change the dielectric properties of the ferrite core because it affected only the magnetic circuits associated with the ferrite.

When using CST Microwave Studio for numerical modeling, the gapped ferrite choke may be replaced by an equivalent choke with no gaps. This substitution reduces the computational resources since narrow gaps require substantial increase in the number of discretization cells. However, the permeability of this new equivalent ferrite will be different from that of the original.

The effect of the gap on permeability was taken into account through the reluctance of the magnetic circuit:

$$\rho = \frac{length}{\mu_0 \mu_r(\omega) \cdot Area}\left[\frac{Ampere-turns}{Weber}\right]. \tag{9}$$

Equation (9) is the general formula to retrieve reluctance related to a magnetic circuit, but since there are two air gaps along the complete circle (length of the magnetic circuit), the reluctance must be expressed as:

$$\tilde{\rho}(\omega) = \frac{2\pi \cdot radius - 2 \cdot gap}{\mu_0 \mu_r(\omega) \cdot Area} + 2 \cdot \frac{gap}{\mu_0 \cdot Area}\left[\frac{Ampere-turns}{Weber}\right] \tag{10}$$

Once the reluctance associated with the real ferrite is known, the complex permeability of the equivalent ungapped ferrite can be extracted using

$$\tilde{\mu}_r(\omega) = \frac{2\pi \cdot radius}{\tilde{\rho}(\omega) \cdot Area}\left[\frac{H}{m}\right]. \tag{11}$$

Figures 2.10 and 2.11 compare the dependency of complex permeability on frequency calculated for gaps of 1 mm, 0.1 mm, and 0.01 mm. The dark blue curves in these figures are related to the measured data provided by Laird Technologies. The remaining curves represent the data calculated using equation (11). These curves demonstrate that the presence of gaps degrades the magnetic properties of the ferrite. As gap size increases and static permeability decreases, the cut-off frequency increases, an effect consistent with Snoek's law, described by equation (1).

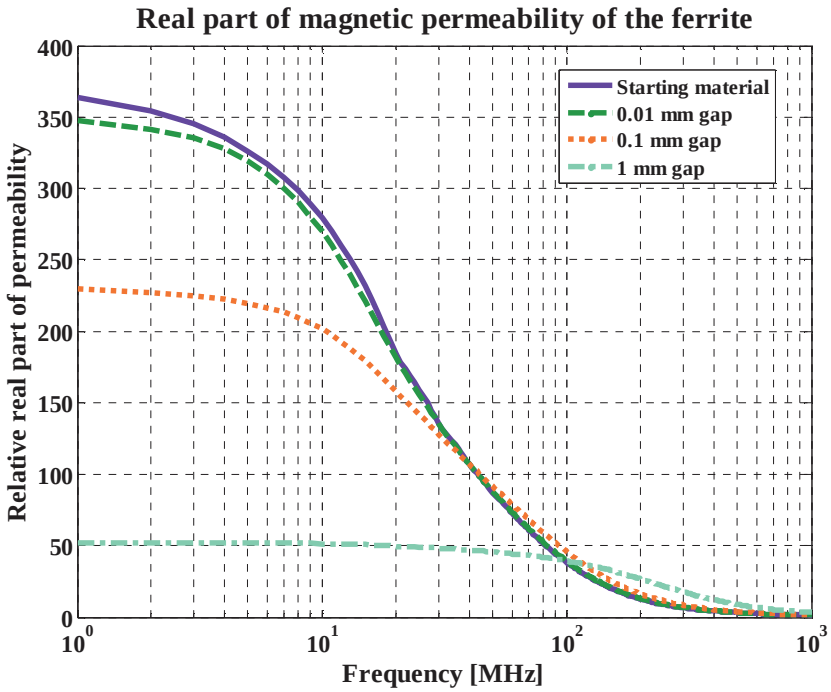

Figure 2.10. Equivalent real part of permeability for ferrite with various gaps.

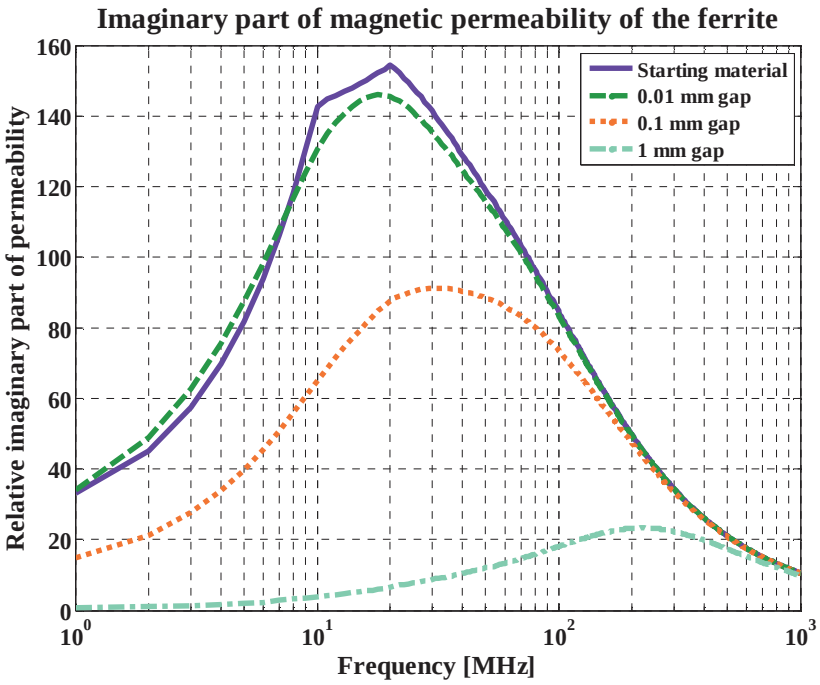

Figure 2.11. Equivalent imaginary part of permeability for ferrite with various gaps.

The permeability curves for the equivalent nongapped ferrite cores were directly loaded into the CST Microwave Studio model (as shown in Figure 2.12). The CST solver can have some instability problems when modeling highly-dispersive materials (i.e. those with high values of μ_r and ε_r); selection of the proper fitting scheme; therefore, is important to minimize simulation time. An appropriate fitting scheme was, therefore, selected to approximate the loaded data. For example, two-term Debye dependence, denoted in the CST tool as the General 2nd, was used as fitting scheme.

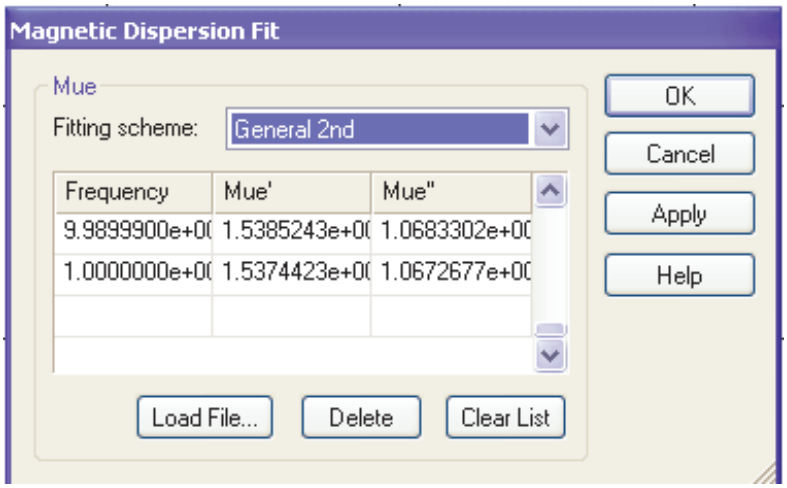

Figure 2.12. Loading material properties in CST.

2.2. INPUT IMPEDANCE EVALUATION

Practically speaking, no model can address all the details present in a real-world problem. Therefore, before formulating a numerical model, a problem must be studied from an electromagnetic point of view in order to determine its most critical parts.

Figure 2.13 shows the laboratory test setup used in this work. A ferrite choke surrounded a wire which was elevated above the ground plane in order to simulate a regular transmission line. This wire had to be straight and parallel to the ground plane. Since the ferrite choke was comparatively large (see the dimensions in Figures 2.13 and 2.14), this wire could not be used to create a 50-ohm transmission line that would fit with ferrite dimensions. This test setup used a wire 0.66 mm in diameter suspended 3 cm above the ground plane.

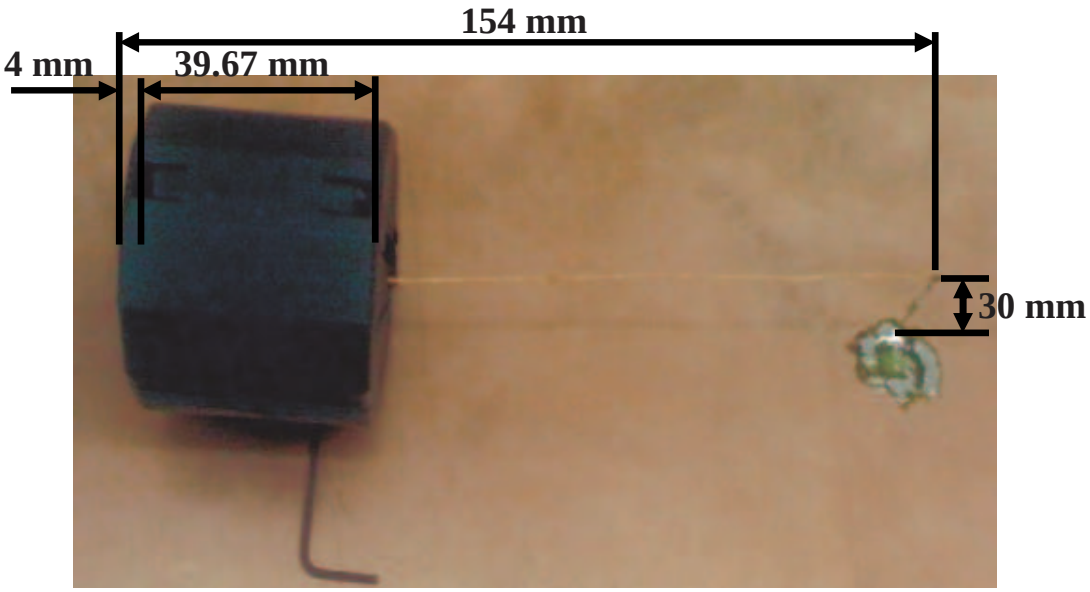

Figure 2.13. Test setup with ferrite along the wire.

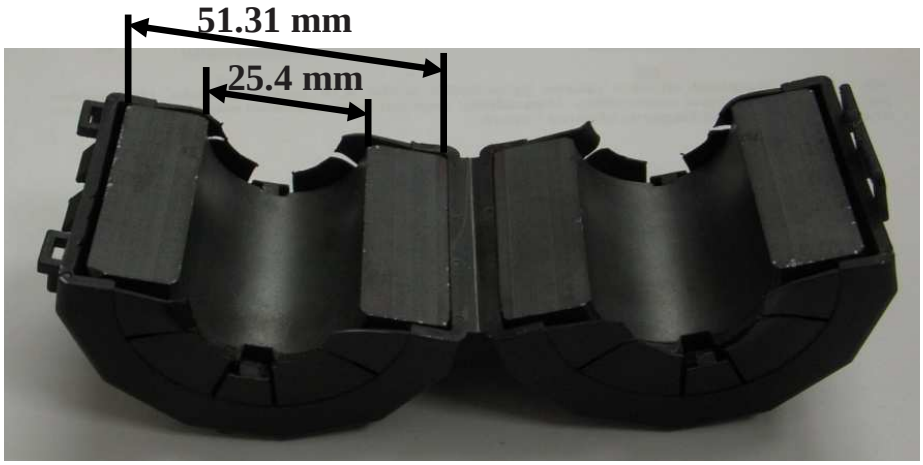

Figure 2.14. Ferrite dimensions.

The lowest reflection occurs when the load and the characteristic impedance of the line are the same. Here, the load termination was chosen to ensure that the reflection from

the load would be as low as possible. This work used an Agilent Infinium DCA-J 86100C time-domain reflectometer (TDR) to inspect the effect of various terminations on system response (i.e., the change in characteristic impedance over time). The flattest response was obtained using a resistor with a nominal value of 290 ohm and a measured value of 295.5 ohm. Figure 2.15 shows a screenshot of the TDR. Since the wire could not be kept exactly parallel to the ground, and since it was not exactly straight, the response from the TDR was not perfectly flat. All simulations and measurements reported below considered a 295.5-ohm load.

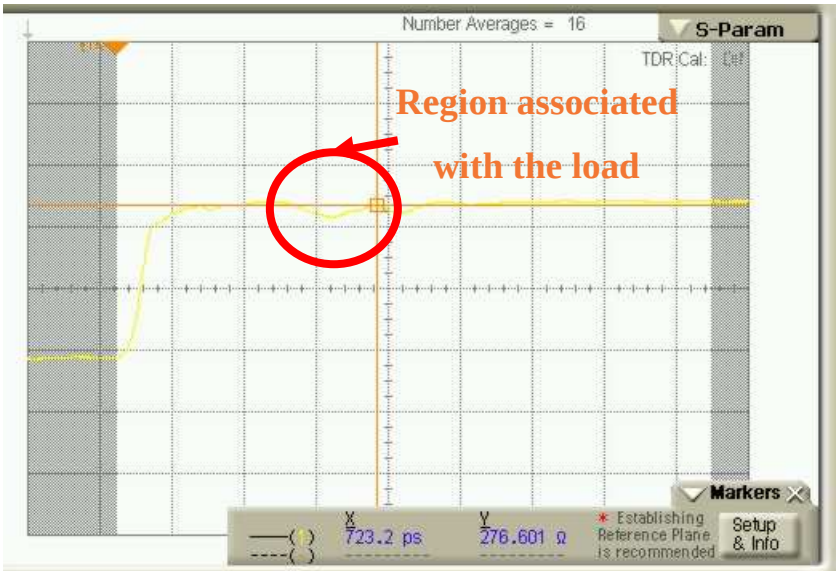

Figure 2.15. TDR measurement.

If a wire over the ground is treated as an air-filled microstrip line [9], its characteristic impedance is described by

$$Z_0(microstrip) = \frac{60}{\sqrt{\varepsilon_r}} \ln\left(\frac{8 \cdot height}{Trace\ width} + \frac{Trace\ width}{4 \cdot height}\right) \approx 371.03\,\text{ohm}, \qquad (12)$$

whereas for a wire above the ground [9] the characteristic impedance is described by

$$Z_0(wire\ \text{above ground}) = \frac{138}{\sqrt{\varepsilon_r}} \log_{10}\left(\frac{4 \cdot height}{wre\ \text{diameter}}\right) \approx 329.44\,\text{ohm}. \qquad (13)$$

The distance from the source to the beginning of the ferrite choke is also important. Here, this distance was 4 mm. As shown in Figures 2.16 and 2.17 the measured input impedance of the ferrite decreases as this distance increases. The real and imaginary parts of the input impedance of the circuit (including the ferrite) were measured using an Agilent Technologies E5071C vector network analyzer (VNA) operating over a frequency range of 100 kHz to 8.5 GHz. This VNA was used because the performance of this Manganese-Zinc ferrite choke was studied over a frequency range of 100 kHz to about 1 GHz.

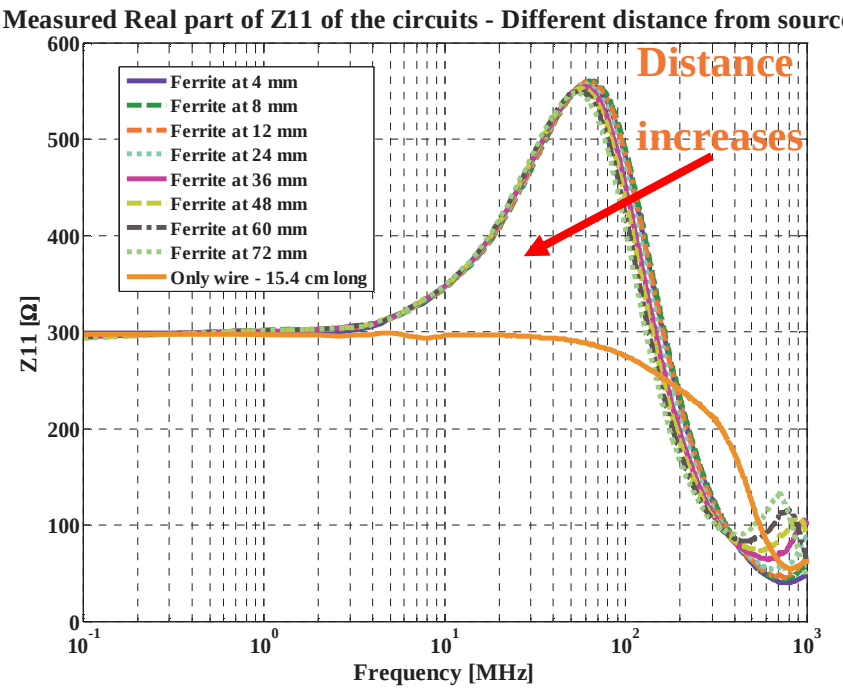

Figure 2.16. Real part of input impedance of the circuit including the ferrite.

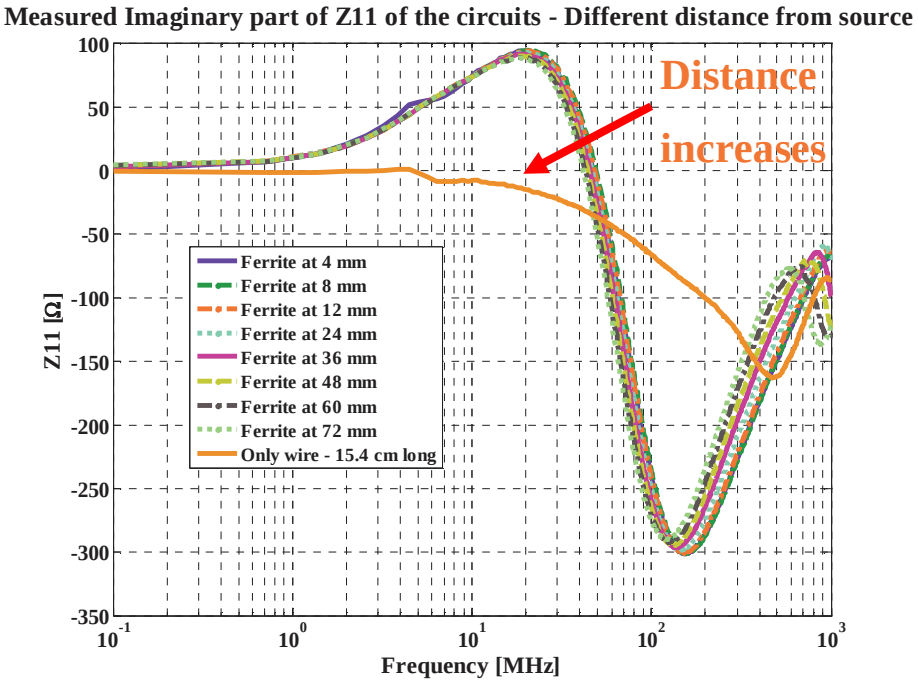

Figure 2.17. Imaginary part of input impedance of the circuit including the ferrite.

The source port was an S-parameter port available in the CST tool, with the 50-ohm impedance (the same as the actual VNA). The port provided the Gaussian pulse shown in Figure 2.18. Figure 2.19 shows the CST model setup corresponding to the measurement test setup shown in Figure 2.13, with the most critical part enlarged.

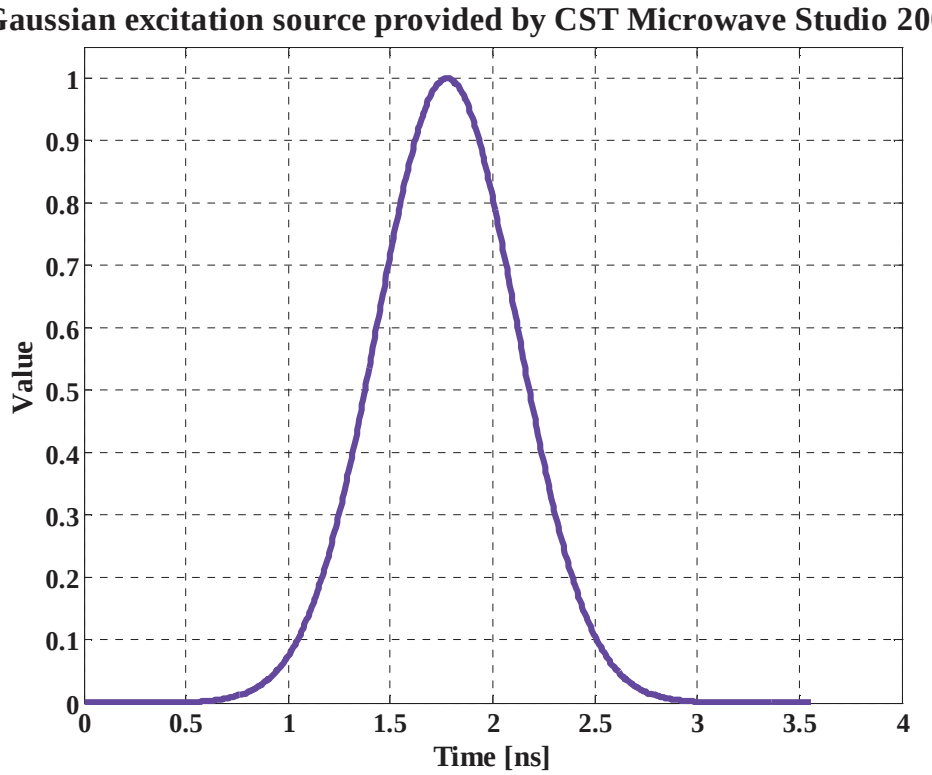

Figure 2.18. Gaussian pulse provided by the 50-ohm S-parameter port.

The load termination was a 295.5-ohm lumped resistance. A port length comparable to the circuit length would have indicated an error because in the CST the length of the port is not considered part of the circuit (wire). In this analysis, the length of the port was 0.05 mm, as shown in Figure 2.19. The model used a wire and ground plane

made of copper. The boundary conditions were open in all the directions to prevent reflection from the boundaries towards the computational domain, similar to perfectly matched layer (PML) conditions.

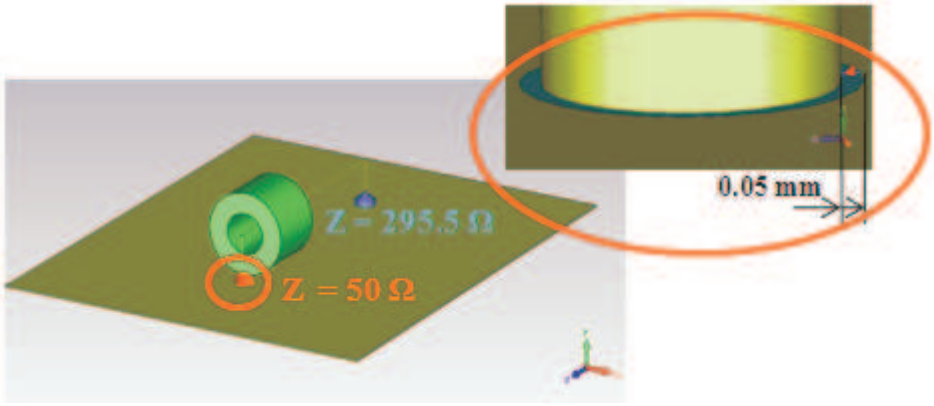

Figure 2.19. CST model representation with focus on port definition.

The problem here was essentially a one-port problem. For this kind of problems Z_{11} (parameter evaluated by VNA and from CST Microwave Studio to estimate performance of a network) and the input impedance Z_{in} coincide. Two sets of measurements and simulations were performed:

- copper wire with a 295.5-ohm load only;
- copper wire with a 295.5-ohm load and ferrite at 4-mm from the source.

Figures 2.20 and 2.21 show the measured and simulated real and imaginary parts of the input impedance. They present the simulation results for various gap sizes in the ferrite choke, together with the case of a wire only (without ferrite). The measured and the

modeled results were most similar for the smallest gap, indicating that the gap in the clamp was really very narrow, only about 0.01 mm.

Once the input impedance data were available from measurements, simulations, or both, the input impedance of the only ferrite choke could be extracted by subtracting the impedance of the wire-only circuit from that of the circuit including the ferrite:

$$Z_{choke} = Z_{total} - Z_{wire}. \tag{14}$$

Figures 2.20 and 2.21 show that the input impedance associated with ferrites of equivalent permeability decreased as gap size increased. The simulation results were also similar for the bulk ferrite with starting material properties and for that with a 0.01-mm gap, but both deviated slightly from the measurement cases. The most significant difference appeared in circuits without ferrite, perhaps because the SMA connector at the port was not modeled in CST Microwave Studio. However, this effect would have been eliminated by subtracting the impedances using equation (14).

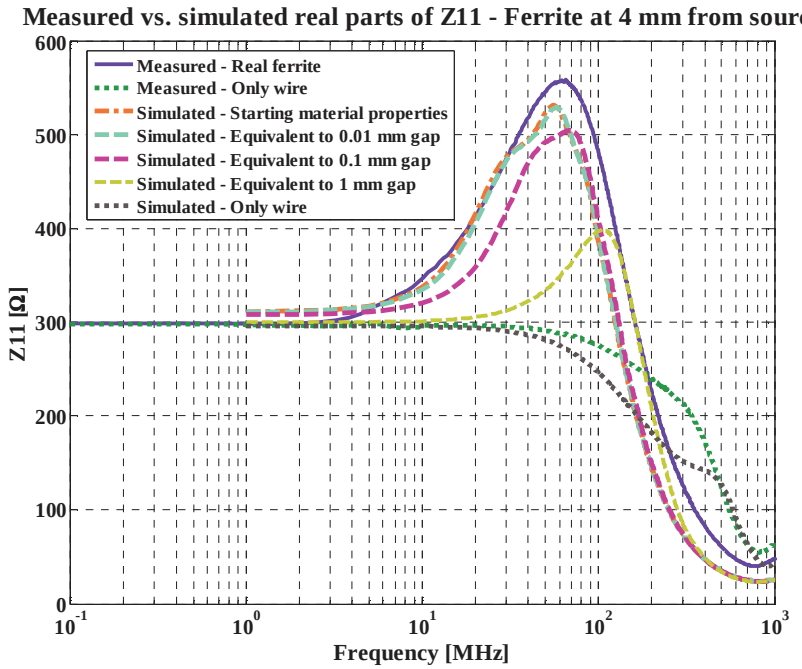

Figure 2.20. Measured versus simulated real components of input impedances.

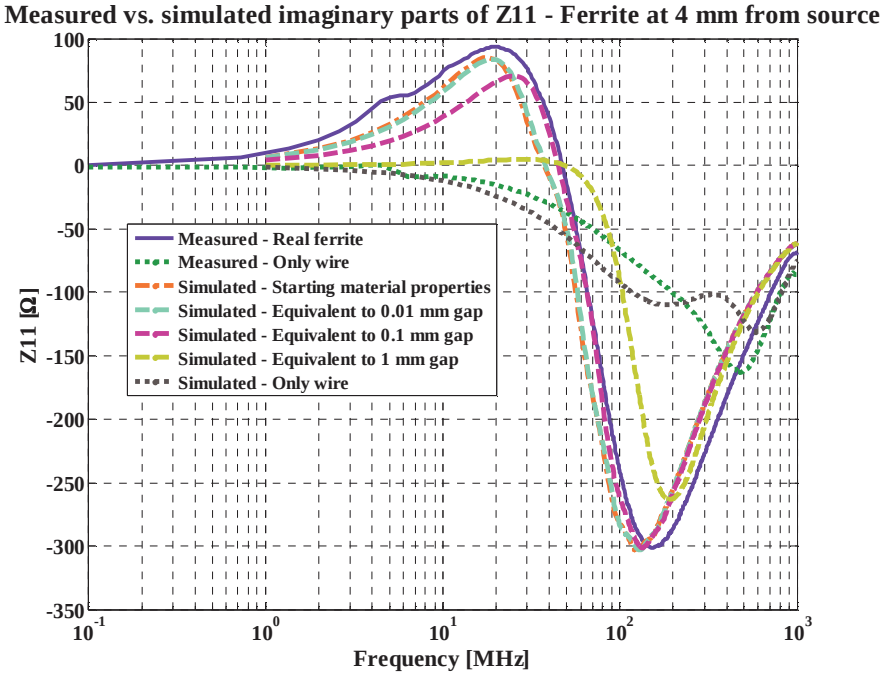

Figure 2.21. Measured versus simulated imaginary components of input impedances.

Figures 2.22 and 2.23 demonstrate the results of this operation, showing closer agreement between measured and simulated results.

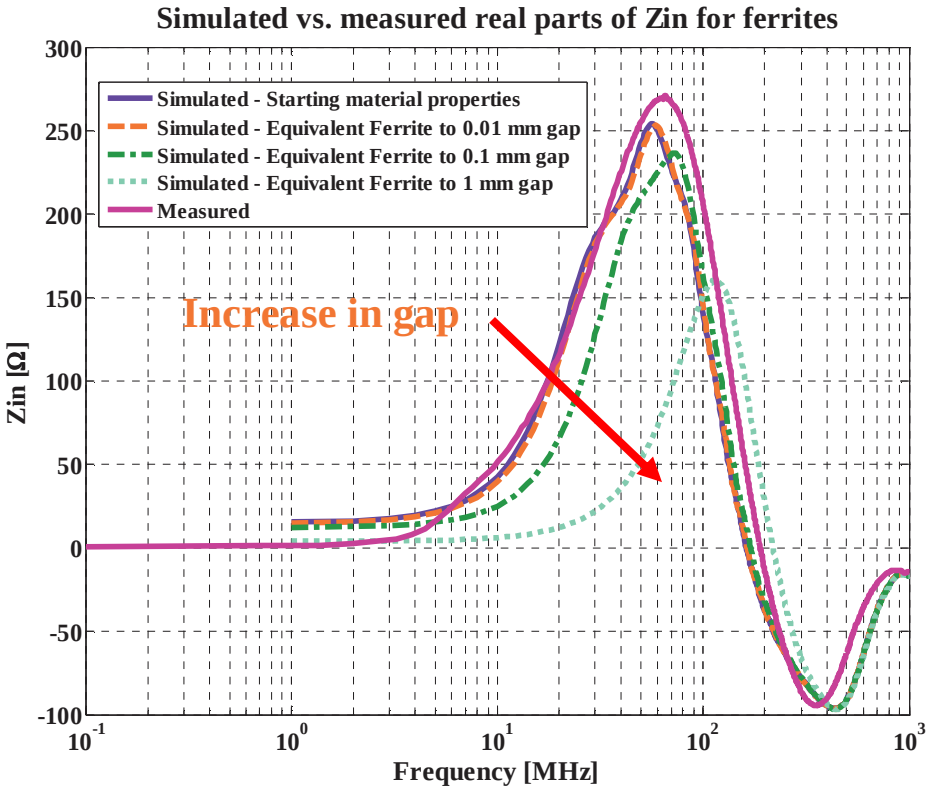

Figure 2.22. Measured versus simulated real components of input impedances after subtracting the impedance of the circuit with load only.

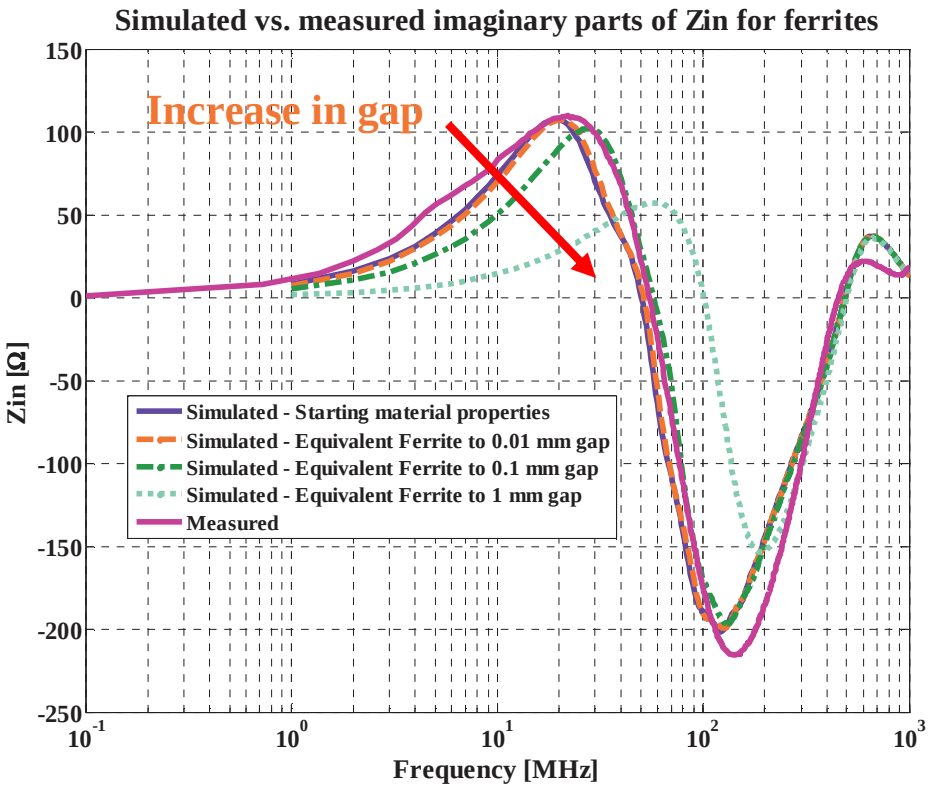

Figure 2.23. Measured versus simulated imaginary components of input impedances after subtracting the impedance of the circuit with load only.

2.2.1. Effect of Ferrite Slicing on Input Impedance. This section compares the input impedance of the full-length ferrite choke and that of choke slices cut along the length. This comparison was intended to verify whether ferrite choke slicing permits cascading of choke impedances in such a way that the resultant input impedance is the algebraic sum of the partial impedances of the slices. This cascading was expected to be possible if the ferrite choke length were small compared to the wavelength propagating along the transmission line structure. CST Microwave Studio software was used to verify this possibility. In the numerical model, the ferrite was cut into three parts of equal length. Slicing the ferrite into smaller lengths caused numerical instability; therefore, the numerical test relied on segments measuring one-third of the total length. Both the real and imaginary parts of the impedance were expected to decrease by a factor of three.

Figures 2.24 and 2.25 present the results of the numerical simulations. Comparison of the input impedance of the full-length ferrite choke with that of the slice demonstrates that the impedance of the ferrite choke depended linearly on its length when the frequency range is below ~200-MHz.

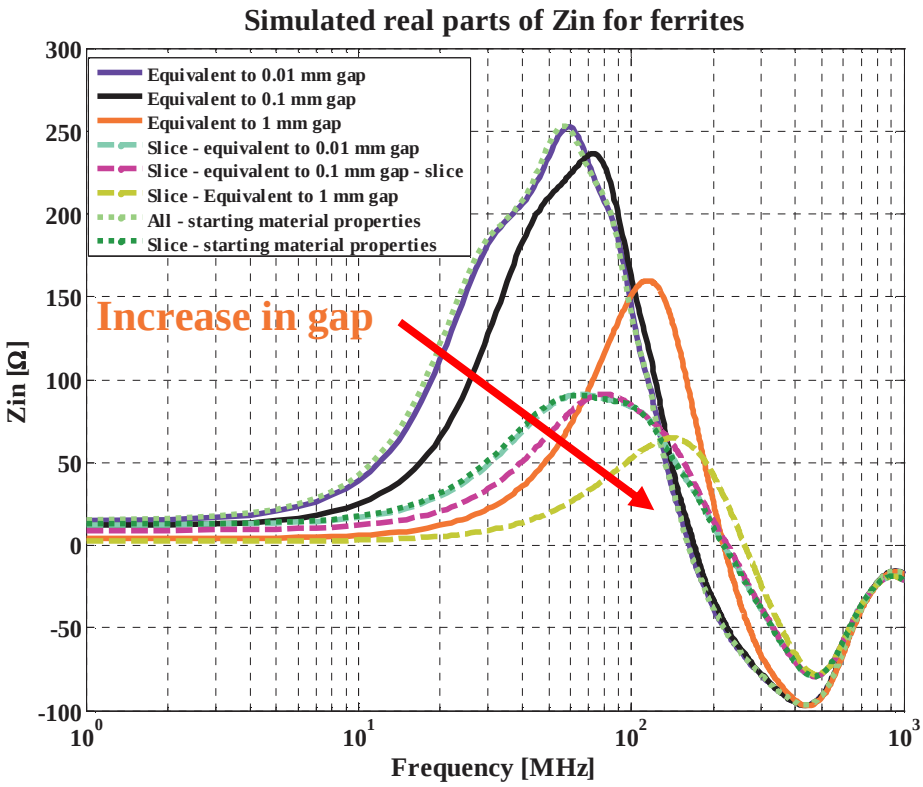

Figure 2.24. Comparison between real component of input impedances for full-length and sliced ferrites.

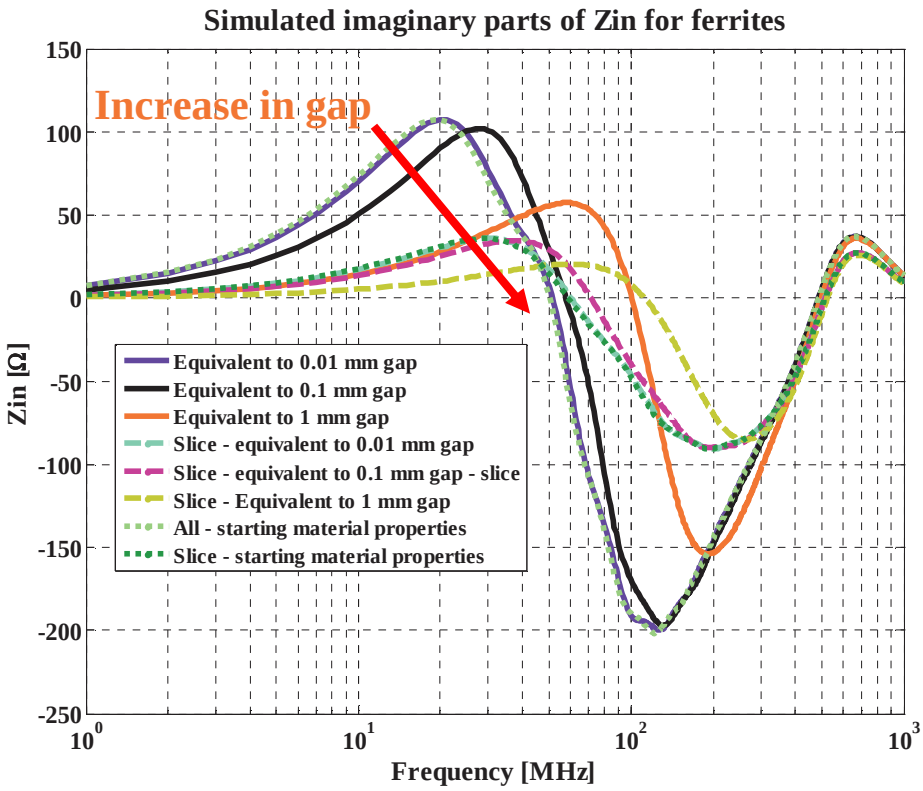

Figure 2.25. Comparison between imaginary component of input impedances for full-length and sliced ferrites.

2.2.2. Effect of Ferrite Movement along the Circuit on Input Impedance. Section 2.2 discusses the effect of the position of the ferrite choke with respect to the source. The following is a more detailed numerical analysis to determine whether the ferrite should be placed near the source or far from it. Some change in the input impedance may be expected due to variation in the distance between the source and the beginning of the choke. Figures 2.26 and 2.27 show the real and imaginary components of the input impedance as functions of frequency for various distances from the source. They indicate that the resonance frequencies and corresponding peak values for both real and imaginary parts of input impedance slightly decrease as the distance between the ferrite and the source increases. This result confirms that ferrites should be placed as close as possible to the source in order to reduce potential CM currents and emissions.

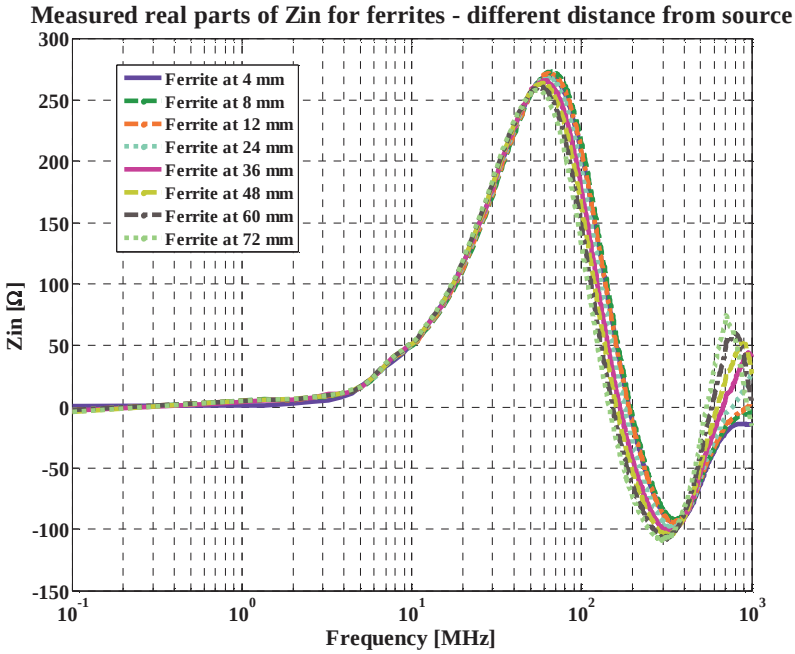

Figure 2.26. Real part of impedance as a function of distance from the source.

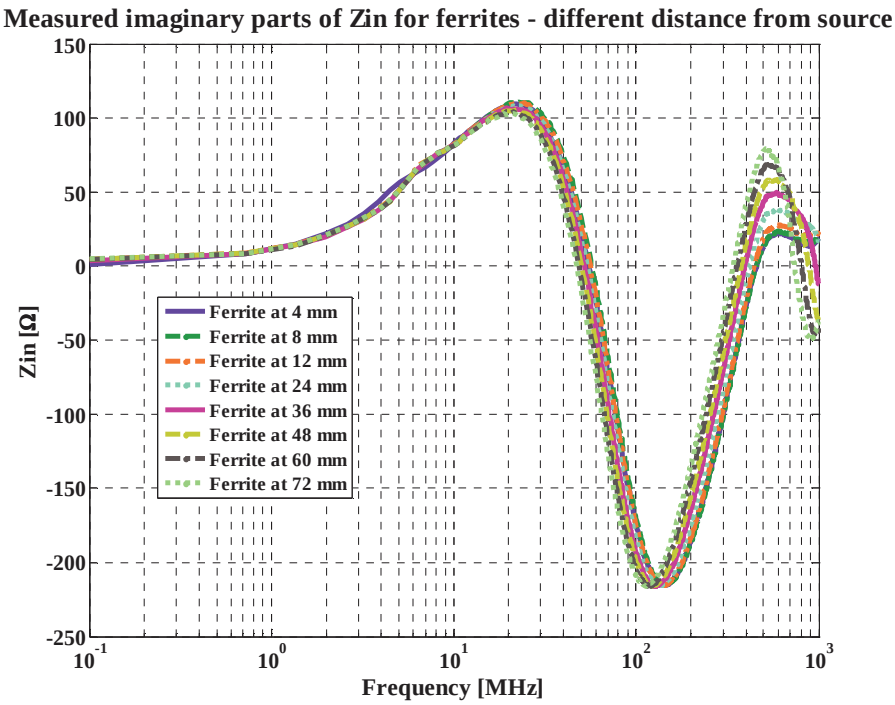

Figure 2.27. Imaginary part of impedance as a function of distance from the source.

2.2.3. Effect of Reduced Circuit Length on Input Impedance. In principle, a reduction in the length of the wire should not affect the input impedance of the ferrite choke. This expectation was verified experimentally by reducing the wire length from the initial 15.4 cm to just 5 cm. Figures 2.28 and 2.29 compare real and imaginary components of impedance for ferrite chokes of two different lengths. As expected, there was almost no difference in the resultant input impedances below 200 MHz.

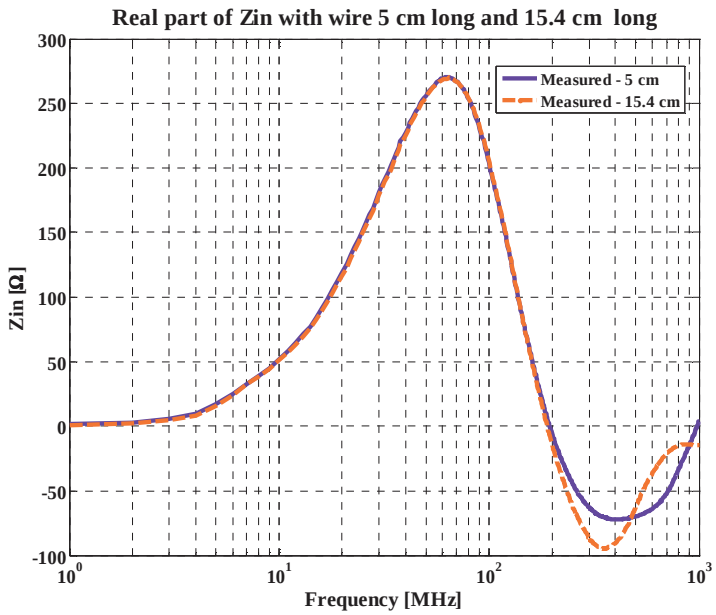

Figure 2.28. Comparison of real components of input impedances with different wire lengths.

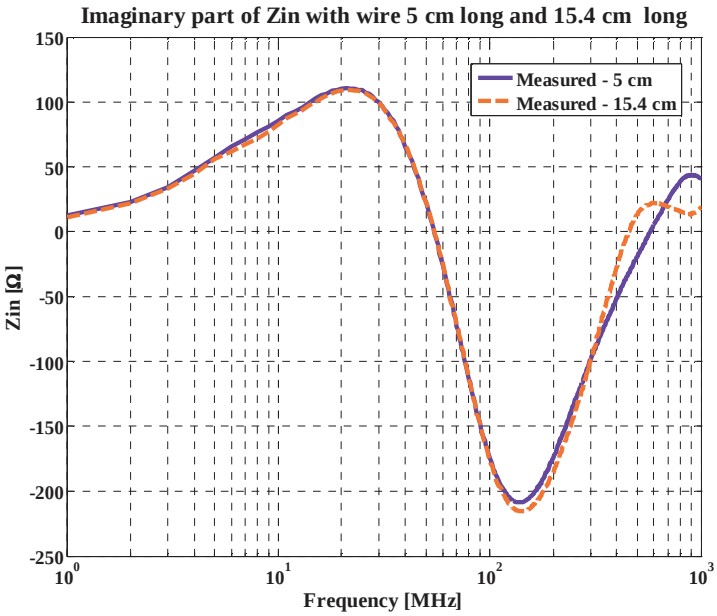

Figure 2.29. Comparison of imaginary components of input impedances with different wire lengths.

2.3. EXTRACTION OF THE EQUIVALENT R, L AND C PARAMETERS

This work sought to extract the equivalent RLC lumped-circuit-elements corresponding to the ferrite choke based on its input impedance components. Figure 2.30 shows the proposed equivalent RLC lumped-circuit. Since dielectric properties of ferrite change little over frequencies ranging from 1 MHz to 200 MHz, the capacitance was assumed to be independent of frequency, in this range. In the same range, however magnetic properties change significantly; therefore, the extracted inductance and resistance were assumed to be functions of frequency. In fact, the equivalent inductance is related to the real part of permeability μ'. The resistance was determined mainly by the frequency-dependent imaginary part of permeability μ'' plus the imaginary part of permittivity ε'', which is almost independent of frequency, and finally by the frequency independent loss in the piece of the wire conductor under the ferrite choke (since at these frequencies the skin effect may be disregarded). At the same time, the equivalent capacitance was determined mainly by the real part of permittivity ε', which was almost constant (Figure 2.9) within the specified frequency range. The assumption that equivalent capacitance is independent of frequency may have been too strong since in reality the capacitance of the choke structure depends not only on the geometry of the choke and the dielectric properties of the ferrite, but also on the position of the internal wire with respect to the ground plane. The latter was disregarded in the present simplified model; however, future work should take into account frequency-dependent capacitance.

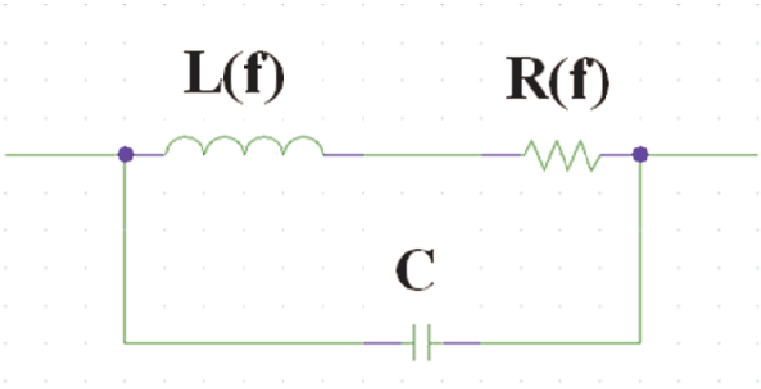

Figure 2.30. Equivalent lumped-element circuit for CM chokes.

Four test cases were chosen for this study: (1) measured ferrite choke; (2) simulated choke with an equivalent ferrite material corresponding to the choke with the 0.01-mm gap; (3) simulated choke with a slice of nongapped ferrite one-third the length of the original; and (4) simulated structure with a slice of equivalent ferrite one-third the length of the original and corresponding to the choke with a 0.01-mm gap. Figures 2.31, 2.32, and 2.33 represent the imaginary part of the input impedance, its real part, and the absolute value, respectively. In Figure 2.31, the region from which the starting value for inductance L_0 was extracted is circled. In Figure 2.33, the region where inductance changed little and was close to L_0 is also circled. This region was characterized by a 20-dB per decade increase in the absolute value of impedance. Figure 2.32 indicates the resonance frequency associated with the resistance value R_{max}. Figures 2.31 through 2.33 also show that the impedance components for the ferrite with the starting permeability and that for the ferrite with the equivalent permeability for the 0.01-mm gapped choke were close. This result is valid for cases of both a full-length ferrite choke and a one-third-length slice.

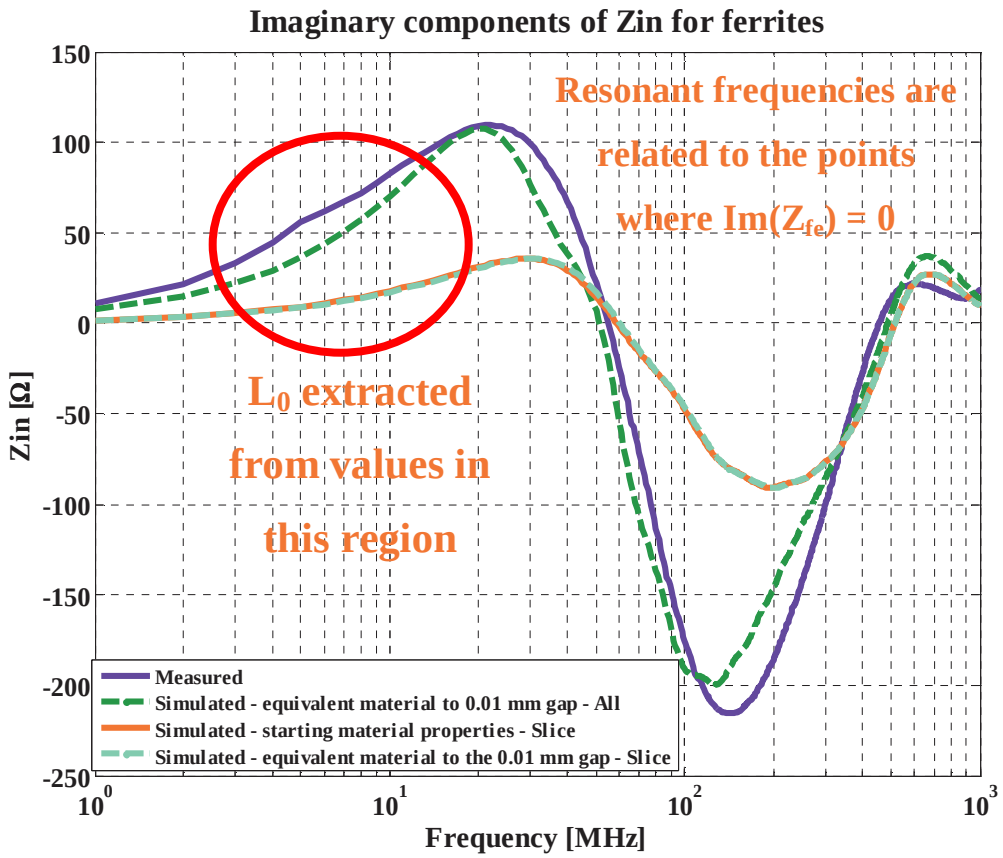

Figure 2.31. Imaginary components of impedances for cases considered in the equivalent lumped-circuit-elements evaluation.

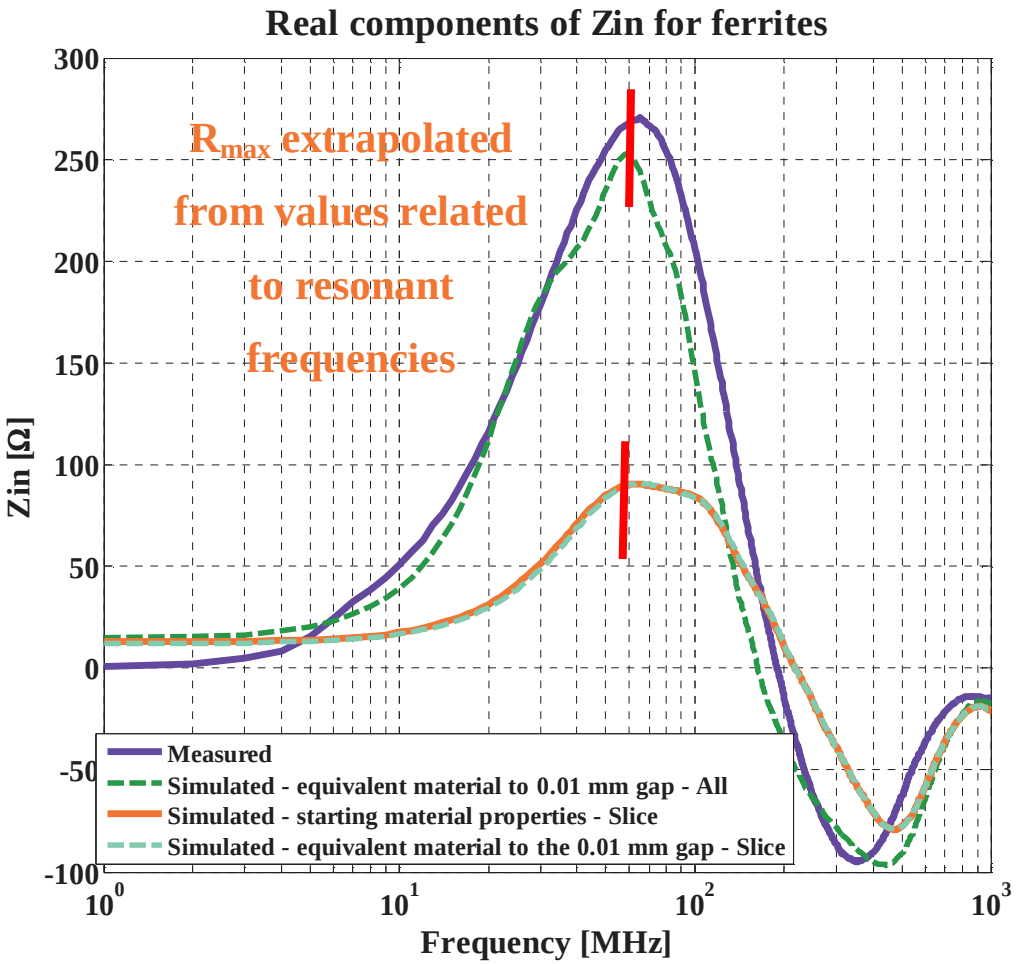

Figure 2.32. Real components of impedances for cases considered in the equivalent lumped-circuit-elements evaluation.

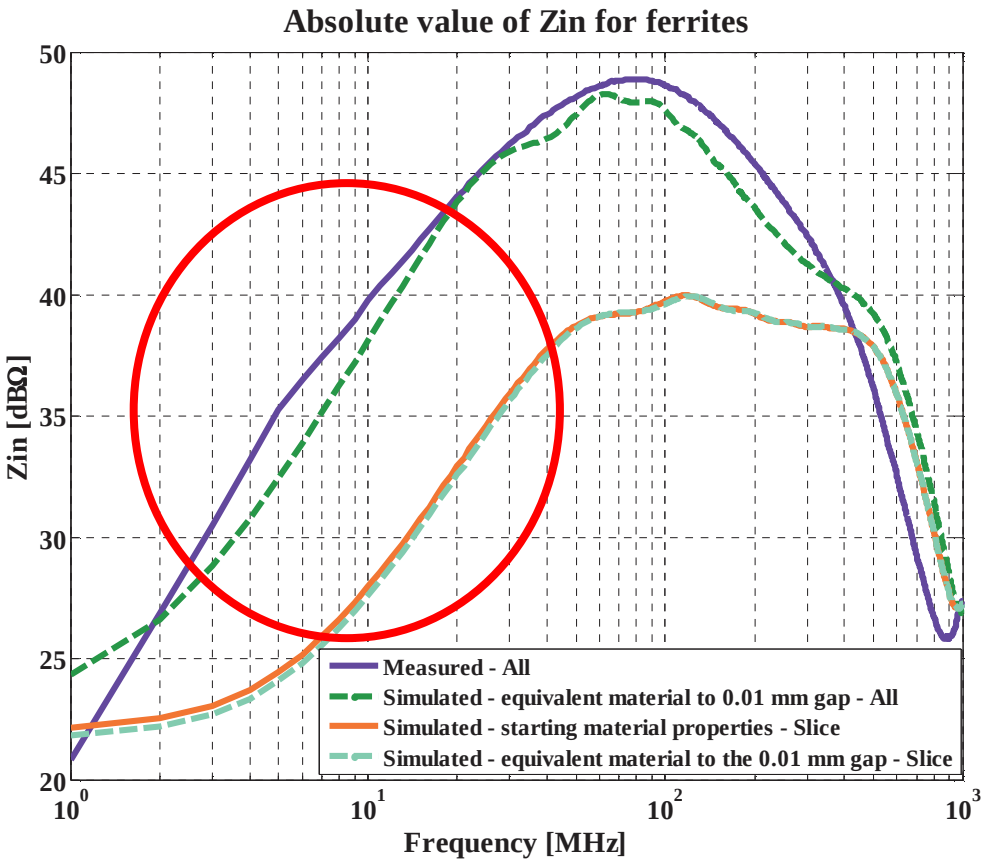

Figure 2.33. Absolute value of impedances for cases considered in the equivalent lumped-circuit-elements evaluation.

The next step for the equivalent circuit parameter evaluation was the extraction of resonant frequencies. Resonance frequency corresponds to the zero of the imaginary part of impedance. Table 2.1 summarizes the resonance frequency results for the four cases discussed above.

Table 2.1. Resonant frequencies extracted from imaginary component of impedances.

	Resonant frequancy [MHz]
Measured case - all ferrite	55
Simulation with material equivalent to the 0.01 mm gap - all ferrite	51
Simulation with starting material properties - slice of ferrite	59
Simulation with material equivalent to the 0.01 mm gap - slice of ferrite	60

The equivalent inductance starting values L_0 for each case were extracted at a frequency equal to one-third of the resonance frequencies since this frequency lay within the 20 dB per decade increase region (see Figure 2.33). The extracted values of L_0 were calculated from the reactance of the ferrite choke:

$$L_0 = \frac{\mathrm{Im}(Z_{fe}(f))}{2\pi f}. \tag{15}$$

The values are reported in Table 2.2. Once the starting inductance values L_0 and the resonant frequency were determined, inductance could be calculated for the entire frequency range:

$$L(f) = L_{\min} + \frac{L_0 - L_{\min}}{1 + \left(\frac{f}{f_{res}}\right)^2} \tag{16}$$

where L_{min} is equal to zero. This equation is proposed to describe the frequency dependence of the inductance since the shape of this dependence was expected to resemble the real part of a Debye curve, as shown by O. Fujiwara [10].

Table 2.2. Frequencies and reactances associated with L_0 extraction (rounded to the nearest whole number).

	Frequency [MHz]	Reactance [Ω]	L0 [μH]
Measured case - all ferrite	18	105	0.98
Simulation with material equivalent to the 0.01 mm gap - all ferrite	17	100	0.99
Simulation with starting material properties - slice of ferrite	20	30	0.25
Simulation with material equivalent to the 0.01 mm gap - slice of ferrite	20	29	0.25

Figure 2.34 shows equivalent circuit inductances as a function of frequency extracted using equation (16). It indicates that the L_0 values for the full-length ferrite and the one-third-length piece are not related by the factor of three. This factor was proved valid for real and imaginary parts of the complex input impedance, but not for inductance and capacitance. They do not depend linearly on the length of the ferrite choke.

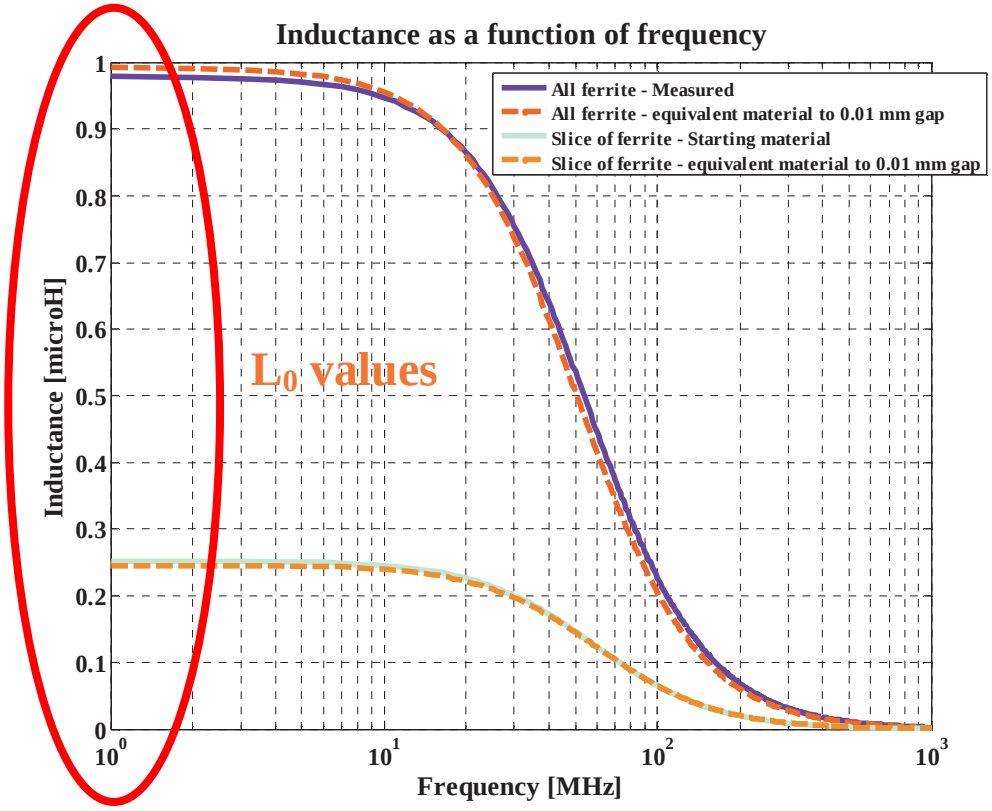

Figure 2.34. Inductances as a function of frequency obtained by using equation (16).

A similar result can be obtained from Fujiwara's equation [10]:

$$Z = \underbrace{j \cdot \omega \cdot L_e}_{\substack{\text{Conductor} \\ \text{Inductance}}} + \underbrace{j \cdot \omega \cdot \left(\dot{\mu} - \mu_0\right) \cdot l \cdot K}_{\substack{\text{Core} \\ \text{Effect}}} \tag{17}$$

where the inductance related to the conductor is

$$L_e = \frac{\mu_0 \cdot l}{2 \cdot \pi}\left\{\ln\left[\frac{l}{a}\cdot\left(1+\sqrt{1+\left(a/l\right)^2}\right)\right]+\sqrt{1+\left(\frac{a}{l}\right)^2}+\frac{a}{l}\right\}, \quad (18)$$

and k is given by

$$k = \frac{1}{2 \cdot \pi}\left\{\ln\left[\frac{D}{d}\cdot\frac{1+\sqrt{1+\left(d/2l\right)^2}}{1+\sqrt{1+\left(D/2l\right)^2}}\right]+\sqrt{1+\left(\frac{D}{2l}\right)^2}-\sqrt{1+\left(\frac{d}{2l}\right)^2}-\left(\frac{D}{2l}-\frac{d}{2l}\right)\right\}. \quad (19)$$

Since the equivalent lumped-element circuit shown in Figure 2.30 is quite different from that proposed in Fujiwara's paper [10], inductances estimated using equation (17) were evaluated using

$$L_{fe}(f) = \frac{\mathrm{Im}\left(j\cdot 2\cdot\pi\cdot f\cdot(\dot{\mu}-\mu_0)l\cdot k\right)}{2\cdot\pi\cdot f}, \quad (20)$$

and the inductance values thus obtained are shown in Figure 2.35. These inductances were used to estimate the shape described by equation (16) and Figure 2.34.

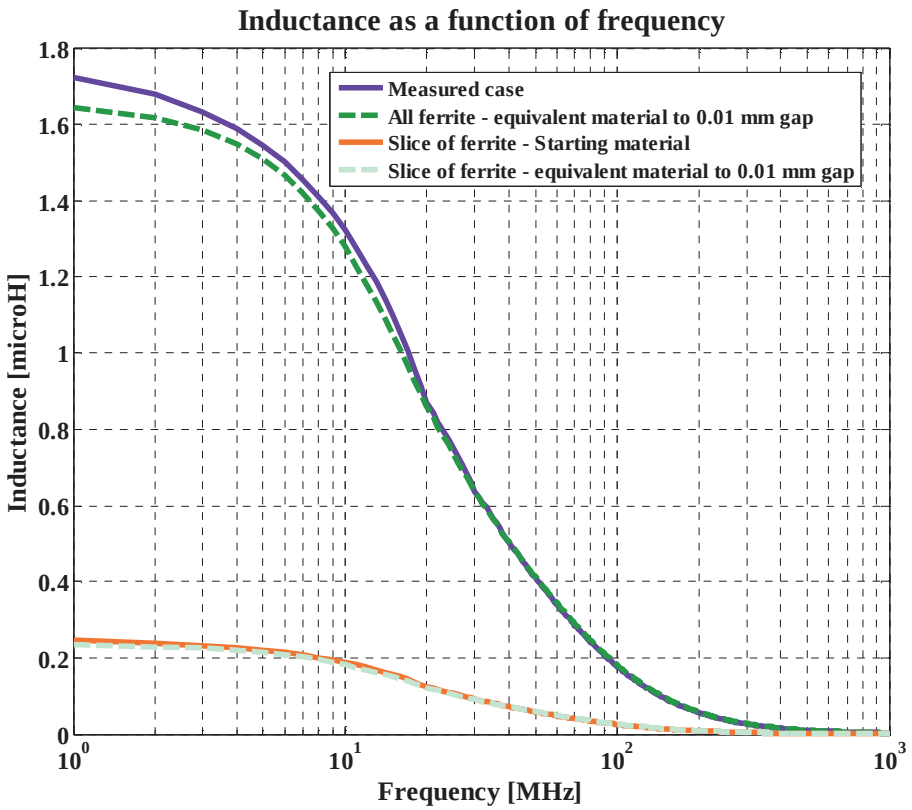

Figure 2.35. Inductances as a function of frequency obtained by using equation (20).

Once the inductances were determined, the equivalent capacitance values could be extracted from the corresponding resonance frequencies:

$$C = \frac{1}{(2\pi f_{res})^2 \cdot L(f_{res})}. \tag{21}$$

As mentioned above, the capacitance values in this model are constant with frequency. Thus, the maximum (resonance) values of resistance could be evaluated:

$$\mathrm{Re}\left(Z_{fe}\left(f_{res}\right)\right)=\frac{L\left(f_{res}\right)}{R_{\max}\cdot C}. \tag{22}$$

Additionally, the frequency-dependent resistance related to the input impedance of the choke could be determined as follows:

$$R\left(f\right)=\frac{2\left(\frac{f}{f_{res}}\right)R_{\max}}{1+\left(\frac{f}{f_{res}}\right)^{2}}. \tag{23}$$

Similar to the inductance case, equation (23) was chosen to represent the equivalent resistance behavior because the trend in resistance values was expected to resemble the imaginary part of the Debye curve. Since Fujiwara [10] considered an equivalent parallel resistance, his results are not comparable with those generated by the model presented here.

Table 2.3 shows the equivalent circuit inductance, capacitance, and resistance values at the resonant frequency for each of the four test cases. Figure 2.36 shows the resistances as functions of frequency evaluated using equation (23).

Table 2.3. Inductance, capacitance and resistance values related to resonant frequency.

	Resonant frequency [MHz]	Inductance [μH]	Capacitance [pF]	Rmax [Ω]
Measured case - all ferrite	55	0.45	8.5	201.8
Simulation with material equivalent to the 0.01 mm gap - all ferrite	51	0.5	9.8	212.1
Simulation with starting material properties - slice of ferrite	59	0.13	2.9	48.6
Simulation with material equivalent to the 0.01 mm gap - slice of ferrite	60	0.12	2.9	47.7

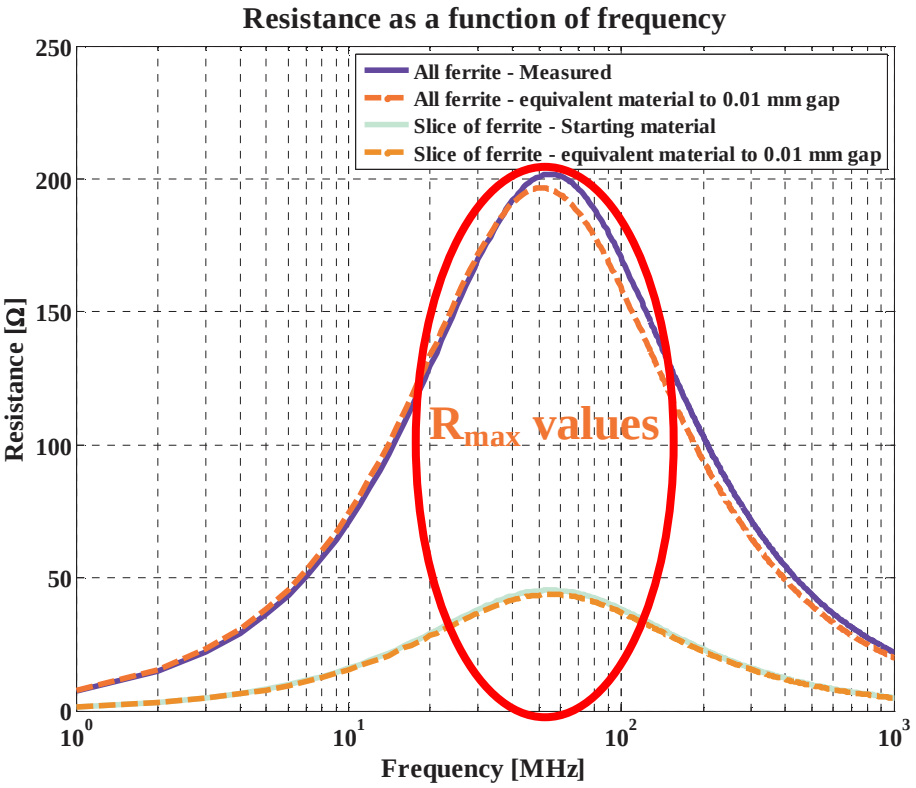

Figure 2.36. Evaluated resistances as a function of frequency.

The next step was to validate the equivalent circuit model for the ferrite choke by comparing the measured or numerically simulated real and imaginary parts of the input impedance with the corresponding input impedance parts restored using:

$$\mathrm{Re}\left(Z_{fe}(\omega)\right)=\frac{R}{\left(1-\omega^2 LC\right)^2+\left(\omega RC\right)^2} \tag{24}$$

$$\mathrm{Im}\left(Z_{fe}(\omega)\right)=\frac{\omega L^2 C\left(\omega_{res}{}^2-\omega^2\right)}{\left(1-\omega^2 LC\right)^2+\left(\omega RC\right)^2} \tag{25}$$

Figures 2.37 and 2.38 represent this comparison. At low frequencies (below 200-MHz), the results showed close agreement between real and imaginary components of the input impedance. Most importantly, the analytical model presented here permitted the matching of resonant frequencies, peak values and the frequencies associated with them.

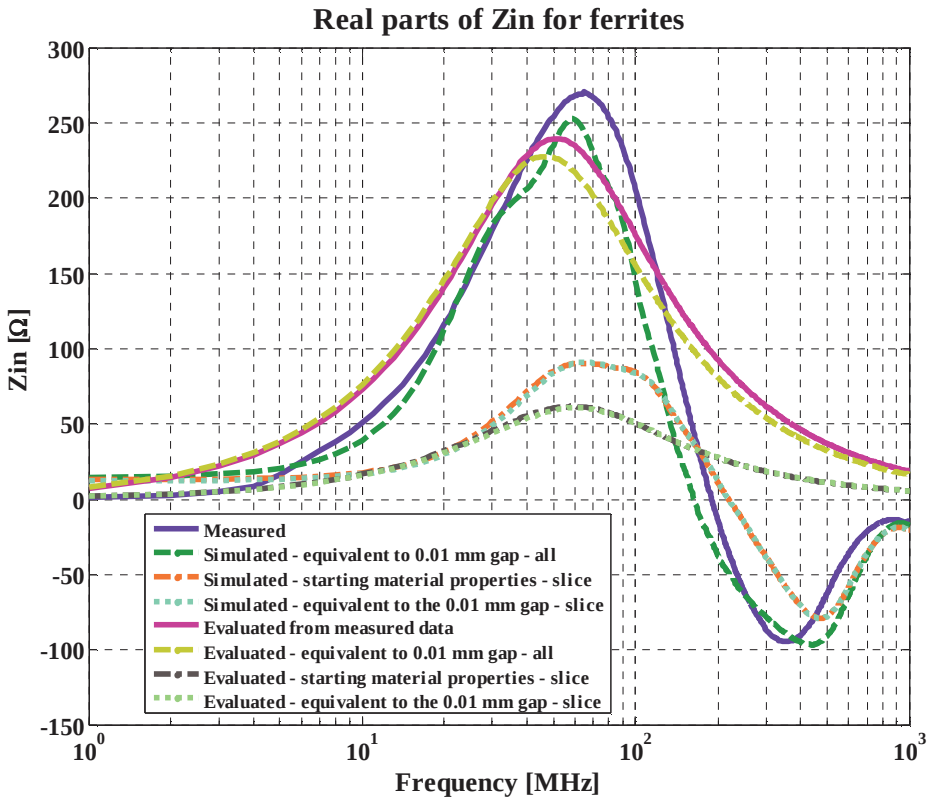

Figure 2.37. Comparison between real parts of input impedance.

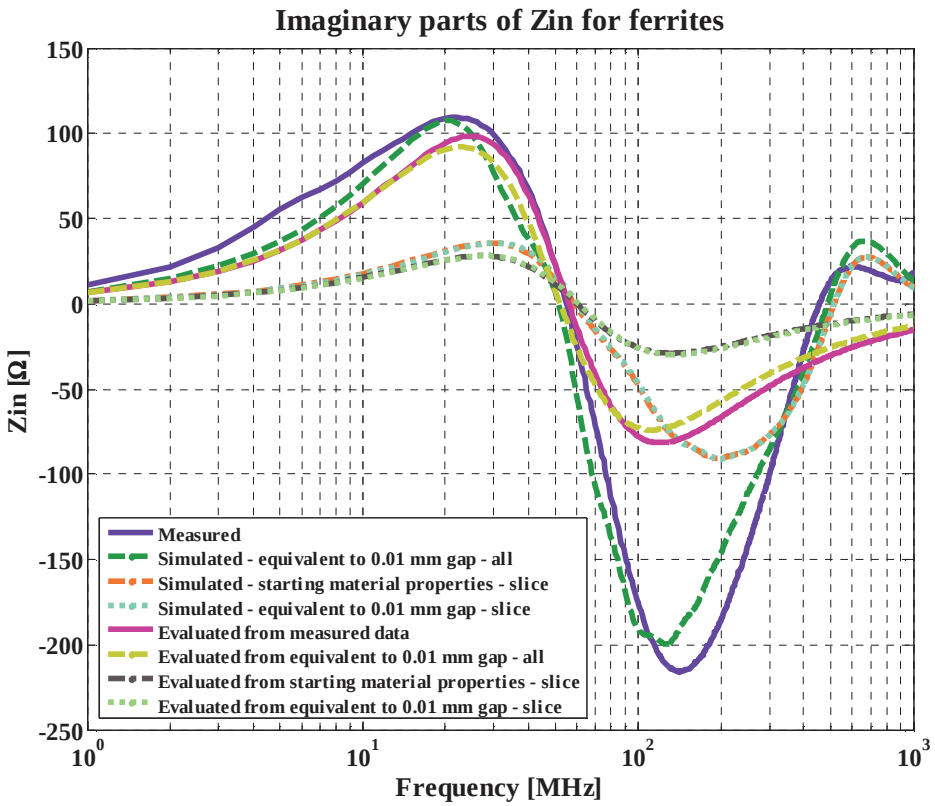

Figure 2.38. Comparison between imaginary parts of input impedance.

The model developed here demonstrates that the real component of impedance must be positive. However, both simulation and measured results show negative values at frequencies above ~200 MHz. There may be a few reasons for this negative-value behavior: First, the simplified analysis assumed that the extracted capacitance was independent of frequency. Second, to evaluate the impedance of the ferrite choke alone, the input impedance of the wire including the ferrite was subtracted from that without ferrite. This subtraction was based on the assumption that lumped-circuit-elements were subtracted. However, since ferrite has high permeability and permettivity values, subtraction is not possible for frequencies above 200 MHz, because wavelength becomes

comparable with length of the ferrite above that frequency. The wavelength associated with 200 MHz is about 5.3-cm with relative permeability value of 50 and a relative permittivity value of 16. The ferrite was about 4 cm long, and lumped-element representation was not correct at high frequencies. The best agreement between the measured and restored results was achieved at frequencies below the resonance frequency, which was ~50/60-MHz here, depending on the test case. For higher frequencies, a ferrite choke requires a more detailed distributed circuit model.

3. SHIELDING MATERIALS

Shielding is a technical measure to reduce electrical, magnetic, or electromagnetic (EM) field penetration into the protected region, as shown in Figure 3.1 [2].

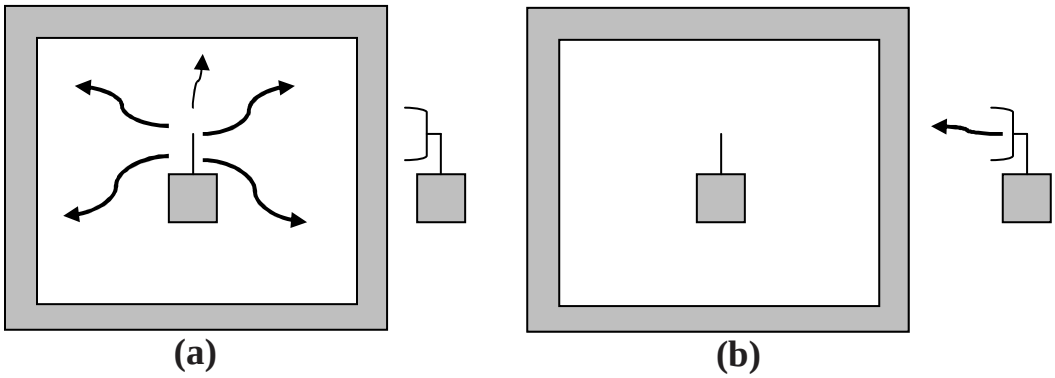

Figure 3.1. Use of shields: (a) to contain emissions and (b) to exclude radiated emissions.

Electromagnetic shielding materials are the structural constituents that contain or prevent the proliferation of EM energy within the bounds of a specific region. The EM shielding materials must meet electromagnetic compatibility/electromagnetic interference (EMC/EMI) requirements.

An EM shielding material is generally selected based on the following criteria:

- ability to provide a given shielding effectiveness (SE);
- suitability for specific shielding applications related to interference due to electric, magnetic, or electromagnetic (radiated) fields;
- geometrical considerations (shape, size, perforation, doors, holes);
- mechanical considerations (rigidity, flexibility, weight, fastening and joints, ability to withstand vibration and mechanical stress, etc.);

- chemical considerations (resistance to corrosion, oxidation, toxicity, etc.);
- thermal stability (performance under hostile thermal environments);
- bandwidth of operation (effective frequency range with acceptable shielding performance);
- simplicity and repeatability in the context of synthesis, manufacturing or processing;
- cost-effectiveness.

In addition, shielding methods can be classified according to the physics of their operation as:

- generating the opposing field;
- diverting the field;
- reflecting the EM radiation;
- absorbing EM energy by various mechanisms of dissipation.

Three phenomena are responsible for effective shielding:

a. Conductive reflection: The time-varying magnetic field component of the incident EM energy induces electric current in the shielding material; these currents provide opposing magnetic fields minimizing the total field beyond the shield.
b. Magnetic reflection: If the shielding material offers high permeability, the magnetic flux lines (time-varying or static) are confined as conductive (low-reluctant) paths through the shield and do not link to the region being shielded.
c. Conductive energy absorption: Energy dissipation in the conductive medium manifests as field attenuation.

Figure 3.2 illustrates two mechanism of shielding against low-frequency magnetic fields: diversion of magnetic flux with high permeability materials and generation of opposing flux based on Faraday's law.

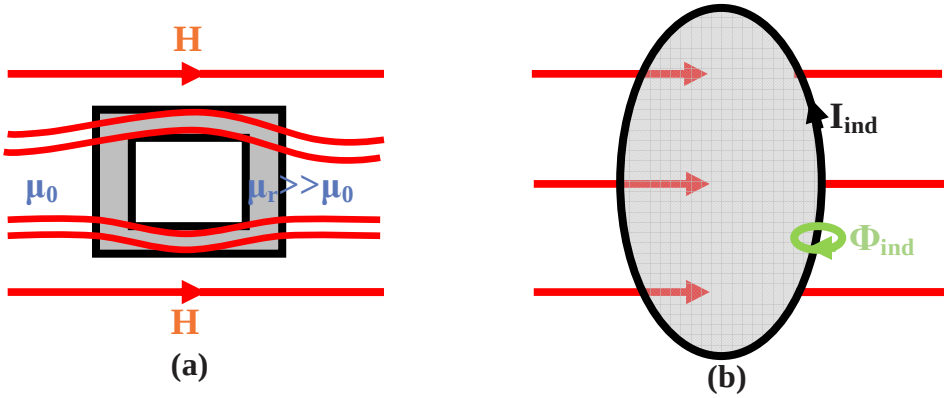

Figure 3.2. Shielding methods against low-frequency magnetic fields: (a) diversion of magnetic flux using a magnetic material, and (b) generation of an opposing magnetic flux by surrounding a magnetic field source with a wire loop.

Traditionally, EM shielding enclosures are made of good conducting materials. A completely closed and highly conductive metal box acts as a very good EM shield. However, real-world electronic device enclosures always have apertures and slots. Slots, seams, and apertures on the conductive surfaces are very good radiators if they cross surface current lines [11]. Also, shielding enclosures made of metals tend to be too heavy. This work considered only single-layered shielding structures.

Analytical and numerical modeling of composite material structures prior to manufacturing saves time and resources during development. To simulate shielding structures made of composite materials using three-dimensional numerical tools the effective electromagnetic properties of composites must be determined. These effective parameters depend on the constitutents of the composite materials. In principle,

composites are inhomogeneous media. Typically, they consist of a homogeneous dielectric base and one or more types of inclusions. However, if incident EM fields have wavelengths much longer than the size of the inclusions, the measured reflection, transmission, and absorption coefficients may be related to the effective, or electromagnetically homogenized, permeability and permittivity of materials.

For shielding purposes, the quality of a material or structure is evaluated based on shielding effectiveness (SE), which can be defined as either far-field or near-field. SE can be evaluated for E-field, H-field, or for total EM power, power flux, or energy.

Far-field shielding effectiveness demands that the distance between the source of emissions and the shielding material is much larger than the wavelength. In this case, the incident wave can be considered as a transverse electromagnetic wave (TEM), as shown in Figure 3.3 [2]. The shielding material is considered as an infinitely wide sheet of finite thickness *t*.

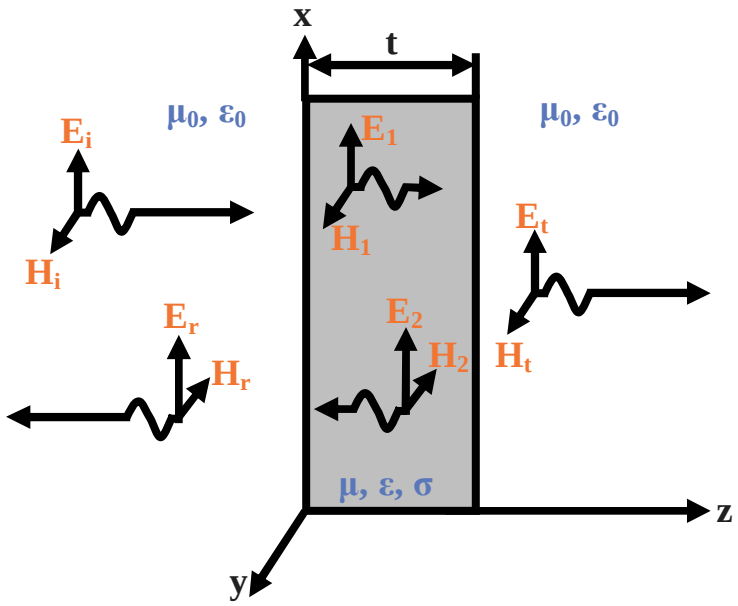

Figure 3.3. Shielding effectiveness of a barrier to a TEM wave.

In this plane-wave formulation, shielding effectiveness can be evaluated as

$$SE_E = SE_H = 20\log_{10}\left(\left|\frac{E_0}{E}\right|\right) = 20\log_{10}\left(\left|\frac{H_0}{H}\right|\right) \quad (26)$$

where E_0 is the magnitude of the incident electric field, H_0 is the magnitude of the incident magnetic field, and E and H correspond to the field transmitted through the shield, as shown in Figure 3.4. Shielding effectiveness values for E and H fields coincide if a plane wave (TEM) is normally incident upon a shield and if both the shield material and the surrounding medium are assumed to be linear, isotropic, and homogeneous. In this case, the electric and magnetic field components are related by the wave impedance of the unbounded medium Z_m, which can be $Z_0 = 120\pi$ ohm in the particular case of vacuum. However, the SE for E and H fields differs in general cases of an oblique incidence, non-TEM modes, and inhomogeneous, anisotropic, non-linear media, or different media on both sides of the shielding barrier. Also, in the case of near fields, equation (26) does not correctly define SE because the relationship between electric and magnetic components is based on more than Z_0.

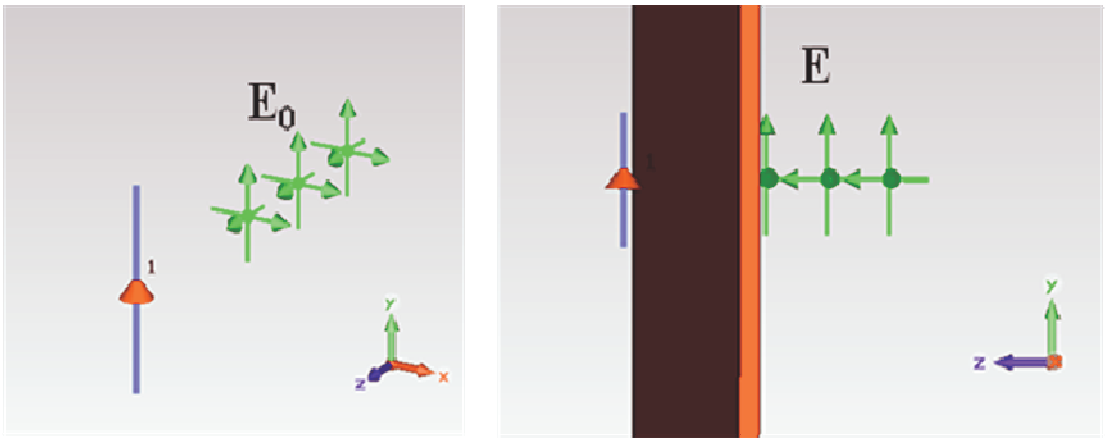

Figure 3.4. Example of CST model to evaluate SE by using equation 21.

Ferromagnetic, ferrite, or ferrite-containing composite magnetodielectric materials provide adequate shielding against far-field sources of EM radiation due to both absorption and reflection losses. Absorption is related to dissipative parts of complex permittivity and permeability of the materials, whereas reflection loss is related to the wave impedance mismatch between the air (or a medium in which an incident wave propagates) and the intrinsic impedance of the magnetodielectric material.

This work computed far-field plane-wave SE for various ferrite-containing materials provided by ARC Technologies. Figures 3.5 and 3.6 show the frequency dependencies of dielectric and magnetic properties of these materials.

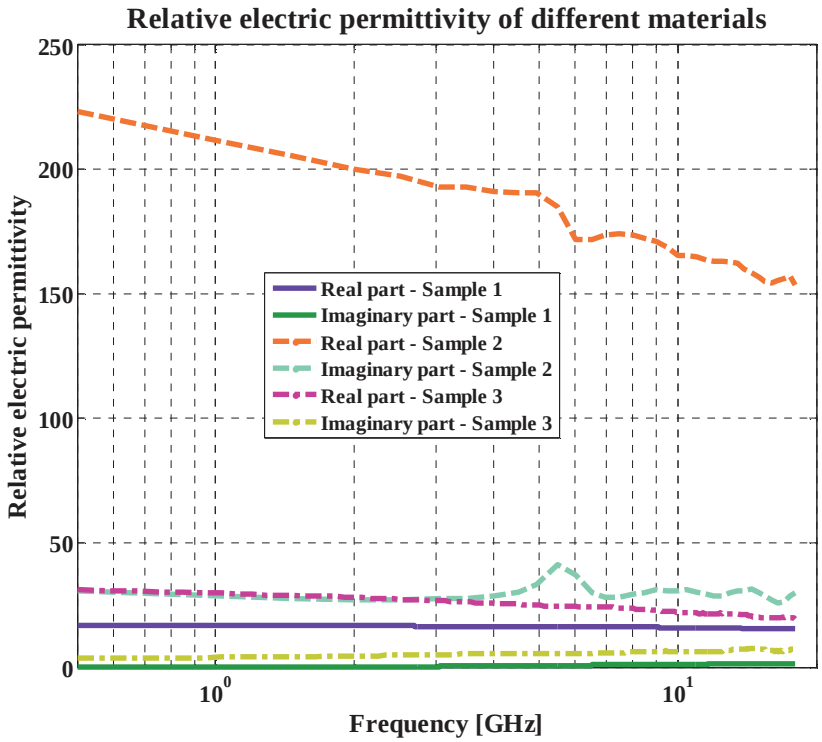

Figure 3.5. Relative permittivity: real and imaginary parts [manufacturer's data].

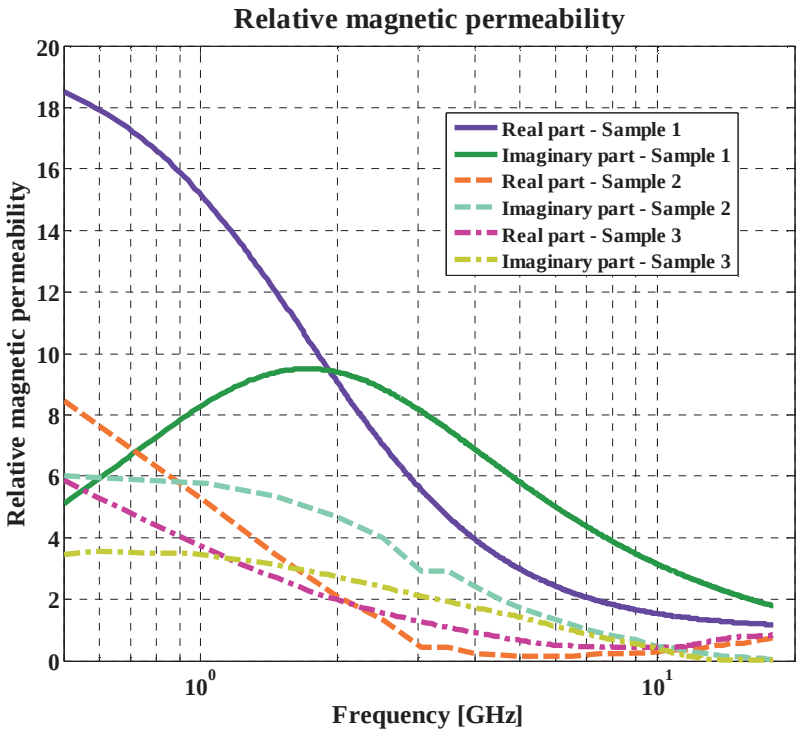

Figure 3.6. Relative permeability: real and imaginary parts [manufacturer's data].

The SE evaluation of a far-field case can be done using simple analytical relationships [12], such as

$$Z_m = Z_0 \cdot \sqrt{\frac{\hat{\mu}}{\hat{\varepsilon}}} \tag{27}$$

$$\gamma_m = j\omega\sqrt{\varepsilon_0 \mu_0 \hat{\varepsilon}\hat{\mu}} \tag{28}$$

$$R_1 = \frac{Z_m - Z_0}{Z_m + Z_0} \tag{29}$$

$$R_2 = \frac{Z_0 - Z_m}{Z_m + Z_0} \tag{30}$$

$$T_1 = \frac{2Z_m}{Z_m + Z_0} \tag{31}$$

$$T_2 = \frac{2Z_0}{Z_m + Z_0} \tag{32}$$

$$T = \frac{T_1 T_2 e^{-\gamma_m l}}{1 + R_1 R_2 e^{-2\gamma_m l}} \tag{33}$$

$$SE = -20\log(|T|) \tag{34}$$

where Z_m and γ_m are the intrinsic impedance of the media and propagation constant related to the material, respectively. In equations (29) through (32), R_1 and T_1 are reflection and transmission coefficients at the first interface (air to absorber), and R_2 and T_2 are the correspondent coefficients for the second interface (absorber to air). Figure 3.7 presents the SE for sheets of these materials as a function of frequency (with parameters shown in Figures 3.5 and 3.6), all 0.03” (0.76-mm) thick.

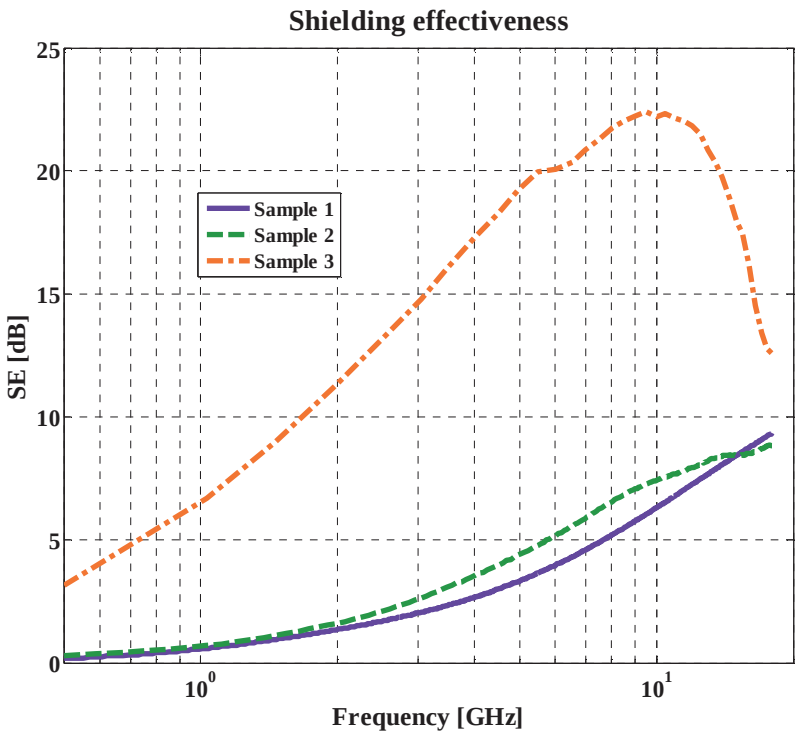

Figure 3.7. Example of SE for far field problem for well defined materials.

Due to their high permeability, ferromagnetic materials and ferrites can also be used to divert or generate an opposing flux for low-frequency magnetic fields [2] related to near-field sources.

To characterize shielding effectiveness in a near-field case the ratios of the E-field or H-field without shield to that with shield has to be considered. However, E and H components are no longer related through Z_0. Figure 3.8 [2] shows the magnitude of the complex "intrinsic wave impedance" $\hat{Z}_w$ of unbounded air for E and H fields as a function of the distance from elementary sources, i.e. electric or magnetic dipoles.

$$\hat{Z}_W(magnetic) = \frac{E_\varphi}{H_\vartheta} = -Z_0 \frac{\frac{j}{(\beta_0 r)} + \frac{1}{(\beta_0 r)^2}}{\frac{j}{(\beta_0 r)} + \frac{1}{(\beta_0 r)^2} - \frac{j}{(\beta_0 r)^3}} \tag{35}$$

This equation and Figure 3.8 [2] demonstrate that SE depends on the type of near-field source (electric or magnetic). The expression for this intrinsic wave impedance would be more complex if the sources of radiation are not elementary dipoles, but some distributed sources of electric or magnetic impressed currents.

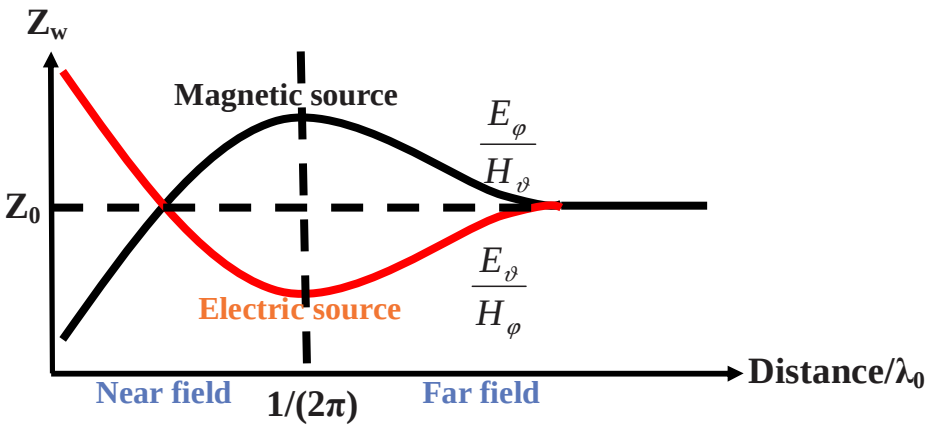

Figure 3.8. Wave impedance at various distances from sources.

When the far-field definition of SE cannot characterize the shielding properties of materials and structures, numerical simulations or measurements are needed. In this work, CST Microwave Studio software was used for numerical modeling. Figures 3.9 and 3.10 show the model setup. Figure 3.9 shows the positions of probes to evaluate fields from

the source (before the first interface) and the fields on the other side of the shield. Figure 3.10 shows the geometry of the magnetodielectric plate under study.

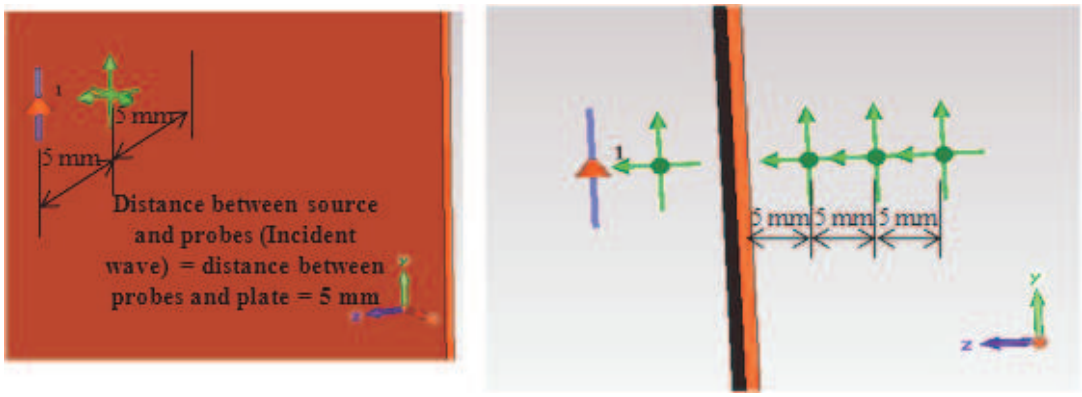

Figure 3.9. Probe positions for incident and transmitted fields evaluation.

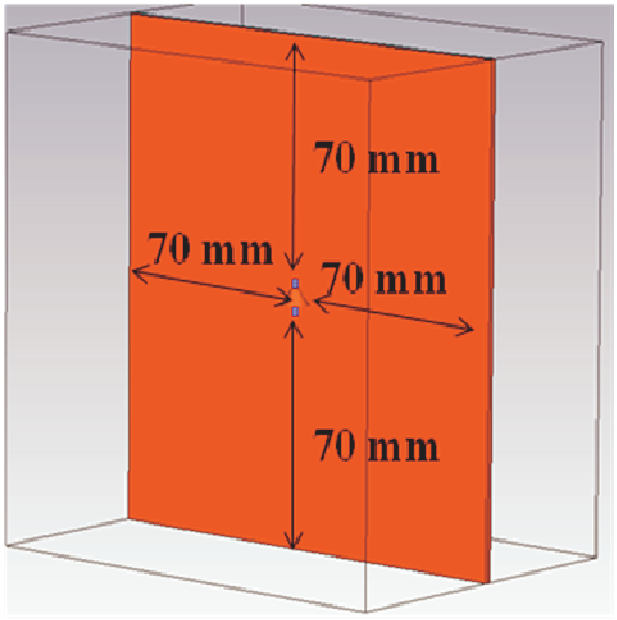

Figure 3.10. Geometry of magnetodielectric plate.

The plate shown in Figure 3.10 is an infinite plate; therefore, boundary conditions for directions related to the largest dimensions of the plate must be close to the perfectly matched layer (PML) conditions, in which all fields go through without being reflected conditions. In CST Microwave Studio this is called open boundary condition. The source is a common S-parameter port with 50-ohm impedance placed very close (10-mm) to the plate in order to represent a near-field source. This kind of source was used to represent a dielectric dipole, and it provided the Gaussian pulse shown in Figure 3.11.

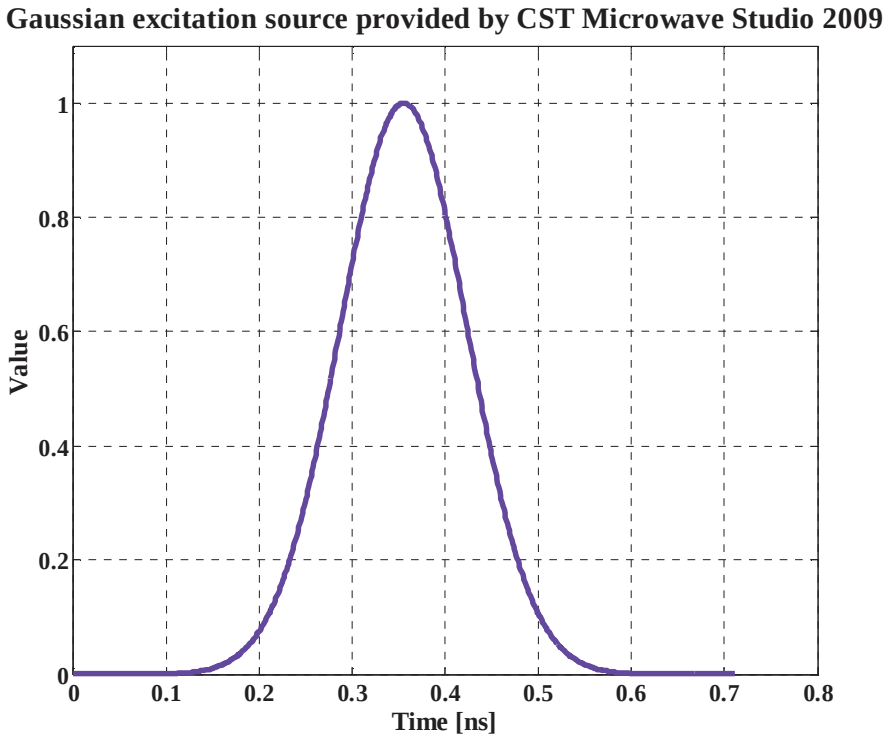

Figure 3.11. Gaussian pulse provided by the 50-ohm S-parameter port.

For near-field approach three different equations permit the evaluation of SE with respect to E-field, H-field, and power. When near-fields are taken into account, shielding effectiveness must be characterized in terms of power rather than fields.

$$SE_P = 10\log_{10}\frac{\left|\mathrm{P}_{\mathrm{incident}}\right|}{\left|\mathrm{P}_{\mathrm{transmitted}}\right|} \tag{36}$$

It can be also evaluated by introducing the notions of absorption and radiation efficiencies in terms of EM power fluxes, as is done by Koledintseva [13].

Using CST Microwave Studio to run numerical simulations, this work studied two samples provided by Laird Technologies. These samples contained different volume fractions of ferromagnetic inclusions (carbonyl iron): Sample 4 contained less carbonyl iron than Sample 5. The permittivity and permeability frequency dependencies were measured by Laird Technologies; they are presented in Figures 3.12 through 3.15. These dependencies were loaded into the CST tool, which curve-fitted them to two-term Debye curves. The latter were used by CST for computations. These approximated curves were close to the original, but they did not completely coincide with the original measured results. The discrepancies between the measured and approximated curves may have led to some deviation of the modeled frequency characteristics of SE from the actual ones.

CST uses a time-domain solver for numerical full-wave electromagnetic computations. These simulations used a Gaussian source with a frequency bandwidth of 5

GHz (Figure 3.11). In the example illustrated by Figure 3.12 thorough 3.15, the low-frequency range was of particular interest because near-field analysis of SE was needed.

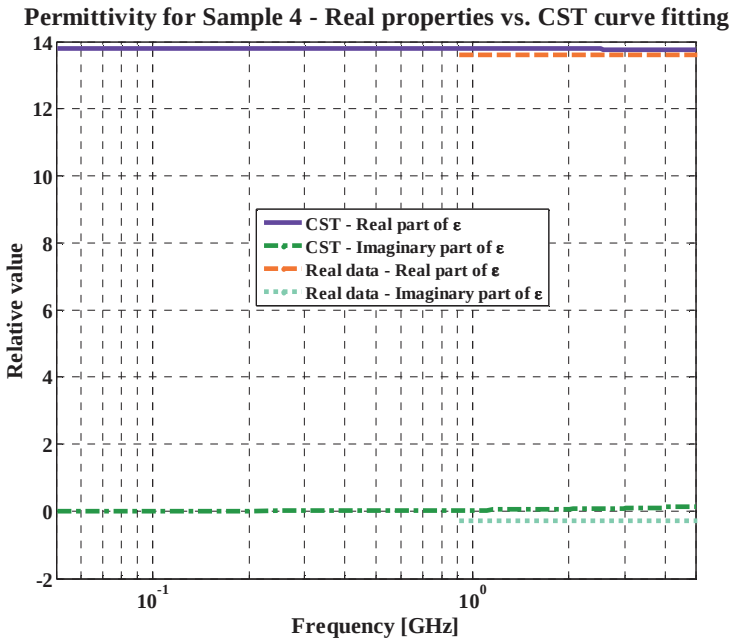

Figure 3.12. Electric permittivity for Sample 4: CST curve fitting versus real data.

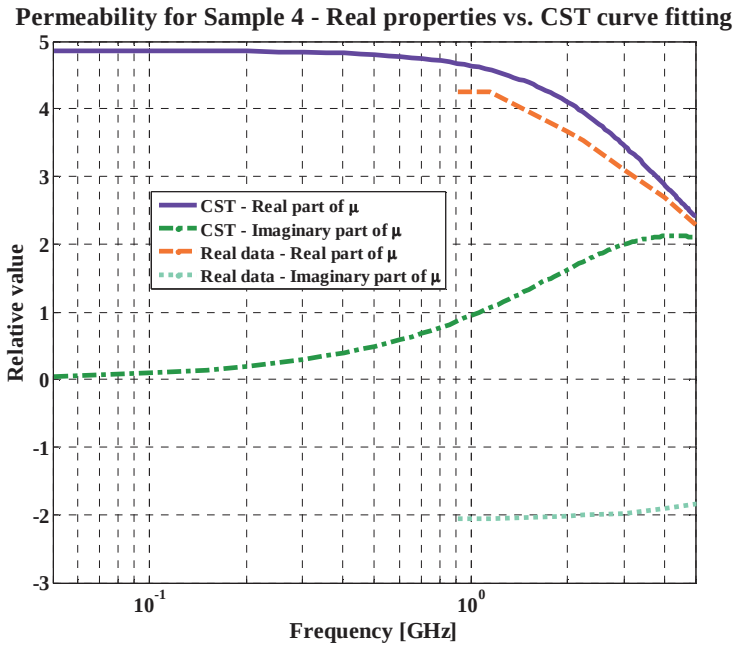

Figure 3.13. Magnetic permeability for Sample 4: CST curve fitting versus real data.

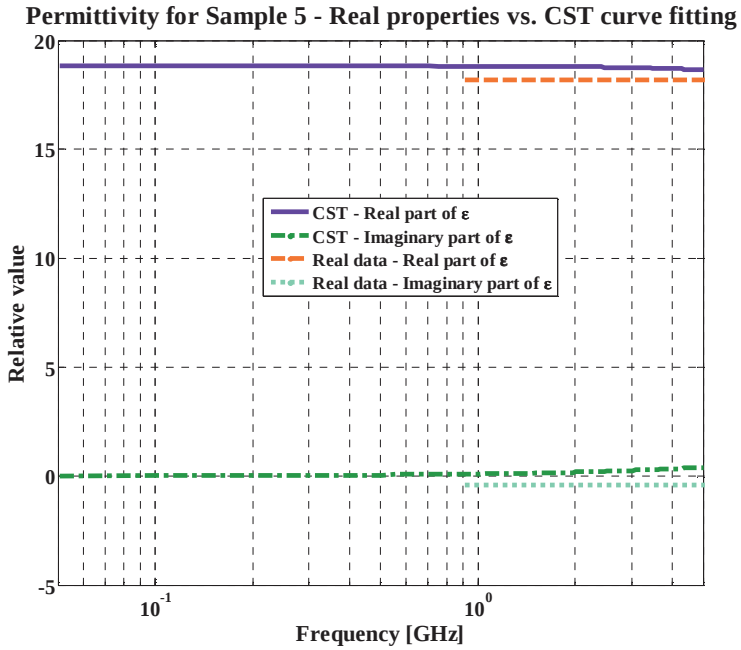

Figure 3.14. Electric permittivity for Sample 5: CST curve fitting versus real data.

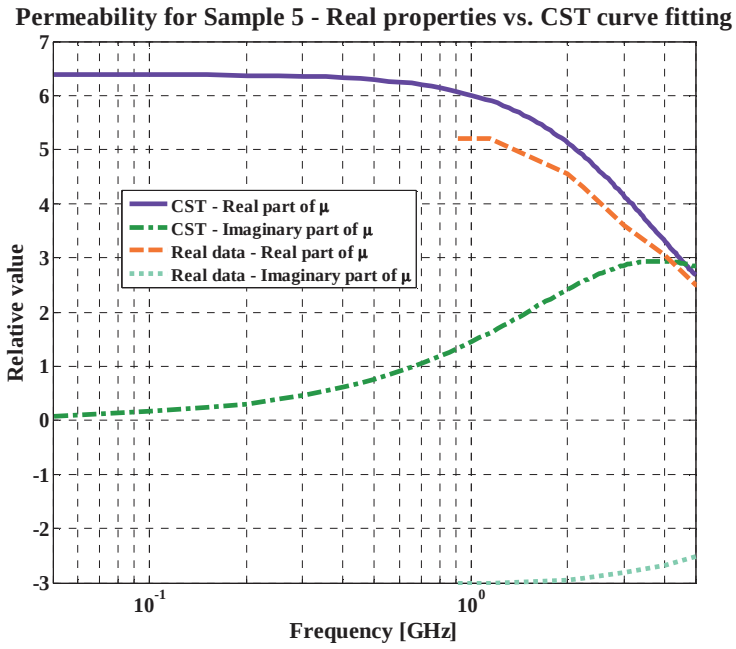

Figure 3.15. Magnetic permeability for Sample 5: CST curve fitting versus real data.

This study addressed two test cases. In the first, the thickness of the shield was fixed at 1 mm. The positions of the source and incident field probes were also fixed; however, the positions of the probes for the "transmitted" field varied with varying the distance from the shield layer. These probes were placed at 5, 10, and 15 mm from the layer, as shown in Figure 3.9.

The second test case used two different thicknesses of 1-mm and 1.6-mm for Sample 4 material; the geometry was the same as in the first test case.

Figures 3.16 through 3.18 show the calculated attenuation of the total magnitudes of E-field, H-field, and power for the first test case. As the distance from the layer to the transmitted field probe increased, the total E- and H-field magnitudes beyond the layer decreased; therefore, the SE values (calculated as ratios of transmitted to incident fields, or

as power) increased. Similarly, Sample 5, which contained more carbonyl iron, showed better SE to both the E and H fields when using the same transmitted probes. This observation did not hold for SE with respect to power across the entire frequency range because the SE did not behave linearly with respect to the h/λ factor [13], where h is the distance between the source and the shield.

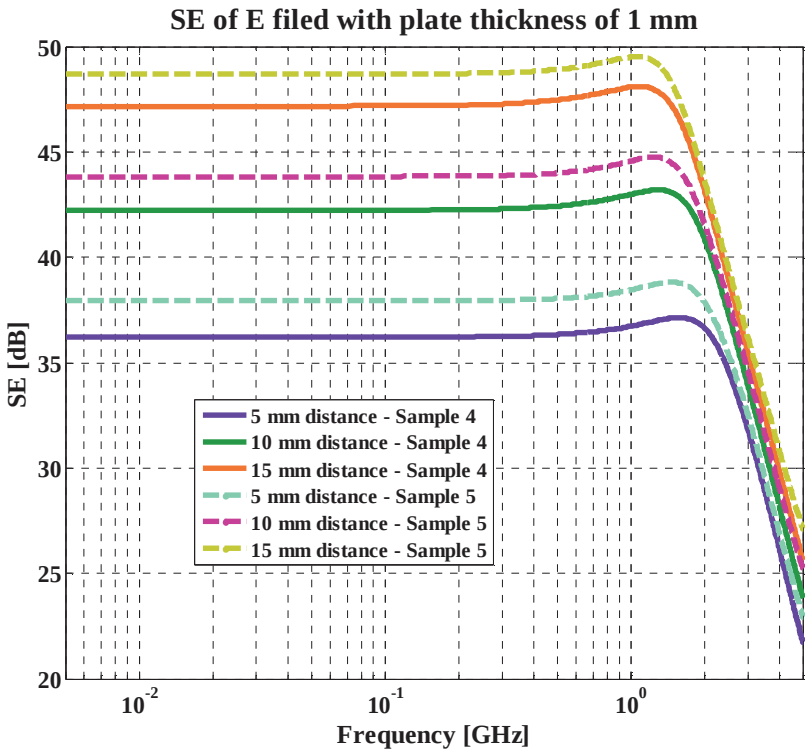

Figure 3.16. SE with respect to E-field as a function of position for transmitted field probes.

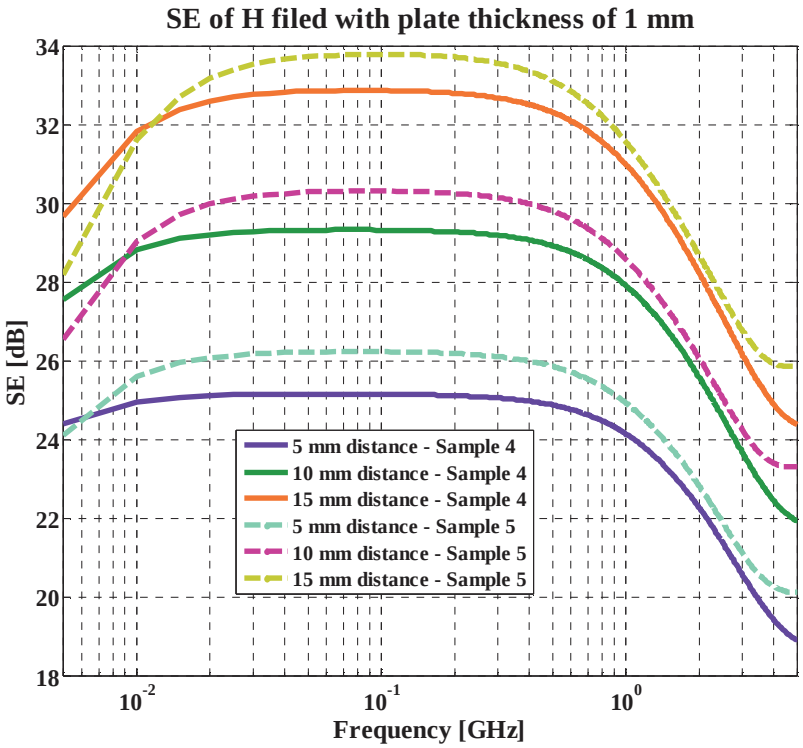

Figure 3.17. SE with respect to H-field as a function of position for transmitted field probes.

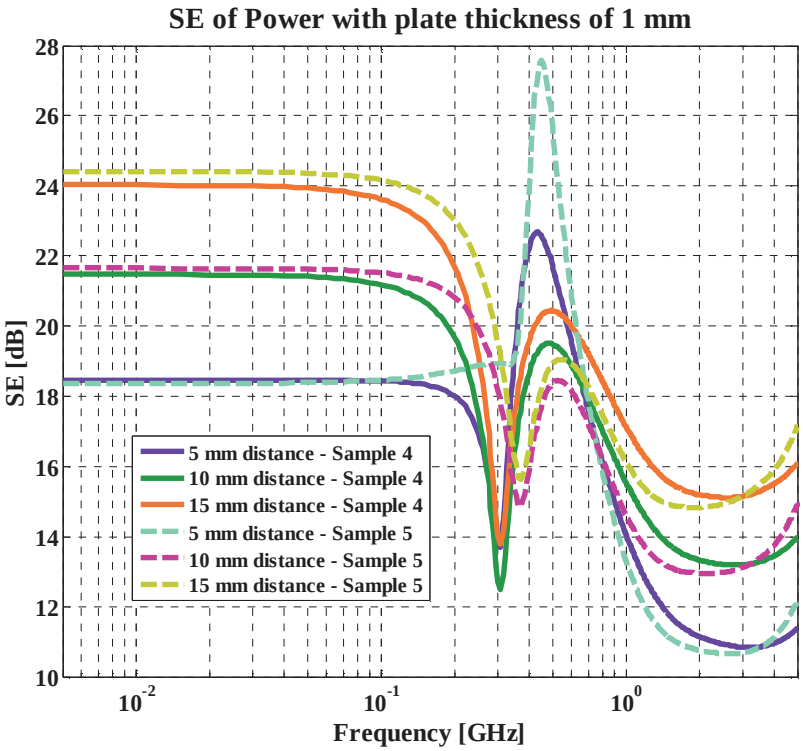

Figure 3.18. SE with respect to power as a function of position for transmitted field probes.

Figures 3.19, 3.20, and 3.21 indicate that if the thickness of the material was increased and all other parameters remained constant, SE also increased with respect to E and H fields. For the same reason identified in the first test case, this did not hold for SE with respect of power across the all frequency range [13].

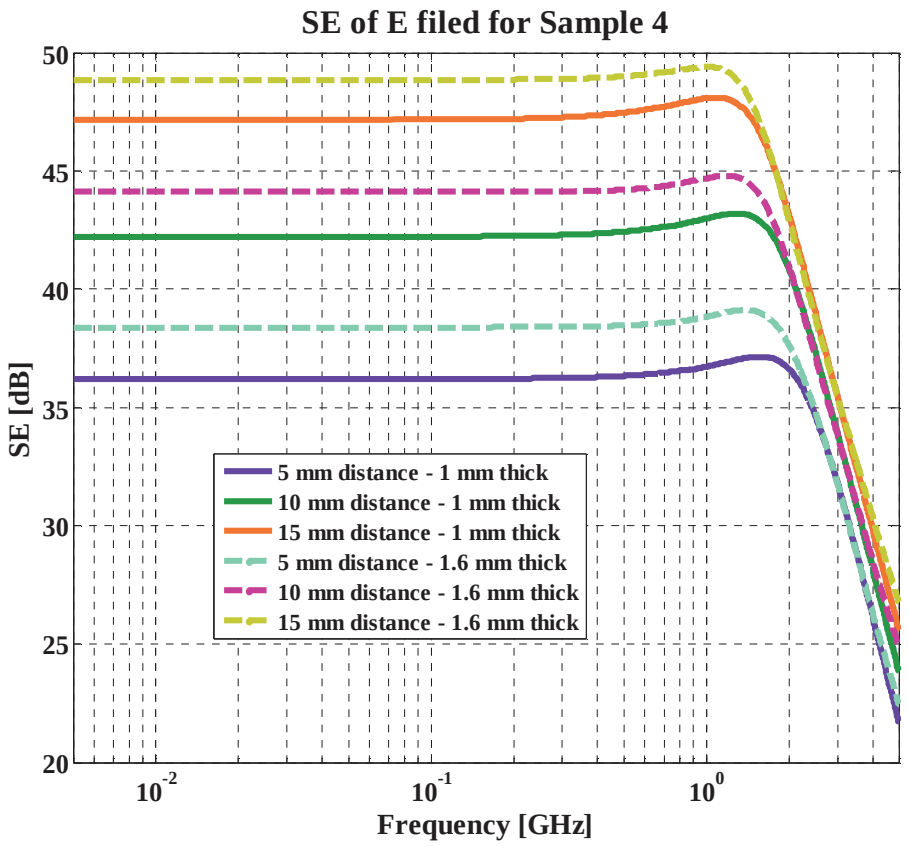

Figure 3.19. SE of Sample 4 with respect to E fields as a function of position for transmitted fields and of shield thickness.

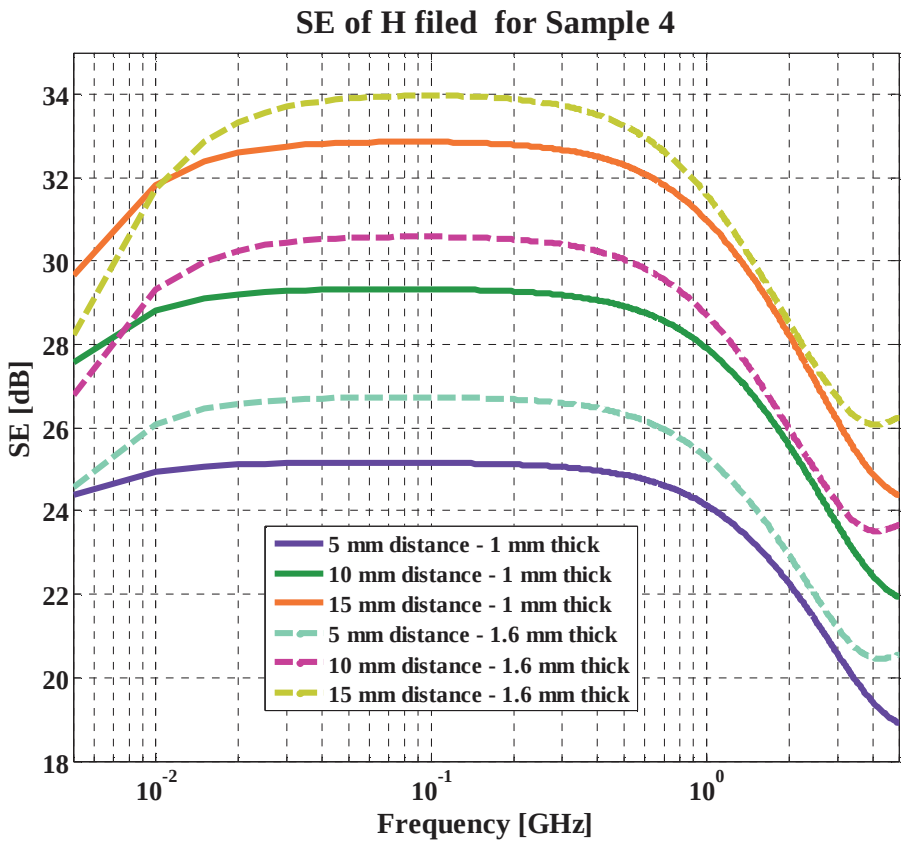

Figure 3.20. SE of Sample 4 with respect to H fields as a function of position for transmitted fields and of shield thickness.

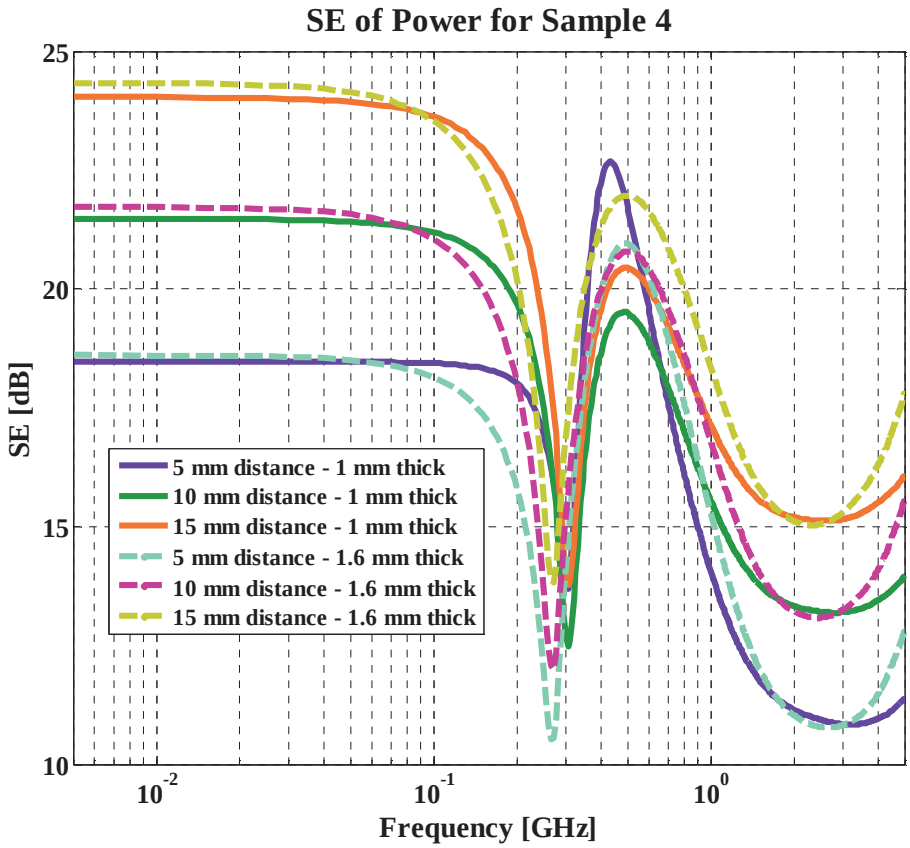

Figure 3.21. SE of Sample 4 with respect to power as a function of position for transmitted fields and of shield thickness.

APPENDIX

COMMON MODE vs. DIFFERENTIAL MODE CURRENTS IN FERRITE CHOKES

A pair of conductors, shown in Figure A.1 [2], carries the currents I_1 and I_2, respectively. Those currents may be decomposed into two auxiliary currents referred as differential-mode (I_D) and common-mode (I_C) currents:

$$I_1 = I_C + I_D \tag{37}$$

$$I_2 = I_C + I_D \tag{38}$$

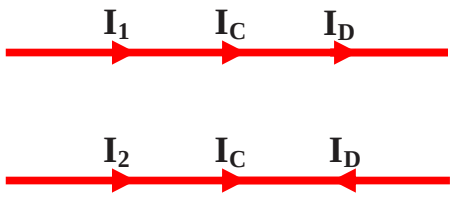

Figure A.1. Current decomposition.

Solving equations (37) and (38), further relationships are obtained as follows:

$$I_D = \frac{1}{2}(I_1 - I_2) \tag{39}$$

$$I_C = \frac{1}{2}(I_1 + I_2) \tag{40}$$

Differential-mode currents are equal in magnitude but oppositely directed, and they are commonly called functional currents. Common-mode currents, on the other hand, are equal in magnitude, and they flow in the same direction. Common-mode currents are not intended to be present; they occur as a result of the usage of switching power supplies.

The radiated electric field E related to each current can be superimposed to give the total radiated electric field. Differential-mode currents are oppositely directed and electric fields display the same behavior of these currents (Figure A.2 (a) [2]). However, since the two conductors are not in the same place but at a defined distance, the fields do not exactly cancel. In the same way, since CM currents flow in the same direction, their radiated fields combine to form a single larger field (Figure A.2 (b) [2]). Thus, a smaller CM current has a much higher potential for producing radiated emissions than does a DM current.

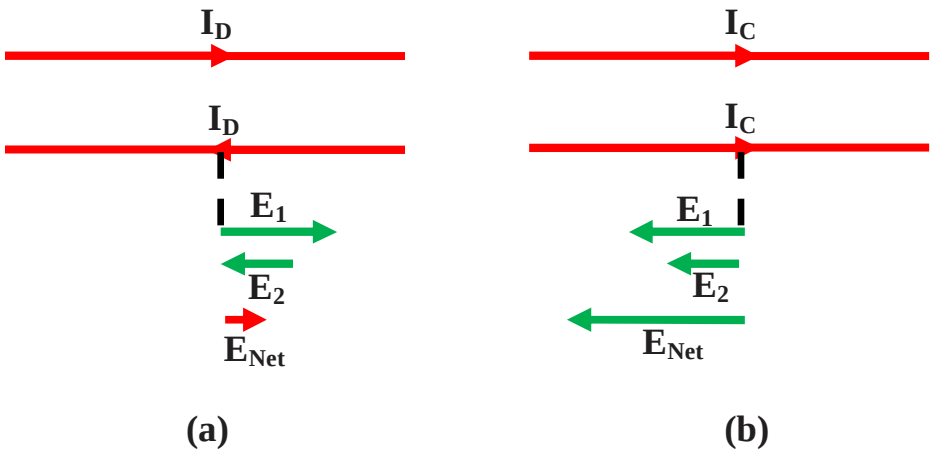

Figure A.2. Relative radiated emission potentials.

A common-mode choke is among the most effective methods for reducing common mode currents. Figure A.3 represents such a choke with related windings [2]. Figure A.3 (a) shows both currents (I_1 and I_2) and the equivalent circuit [2]. Figure A.3 (b) and Figure A.3 (c) show the equivalent DM and CM circuits, respectively [2]. In the equivalent circuits [2], the windings are identical ($L = L_1 = L_2$); therefore, three important relationships can be expressed as

$$Z_1 = \frac{V_1}{I_1} = \frac{j\omega L I_1 + j\omega M I_2}{I_1}, \tag{41}$$

$$Z_{CM} = j\omega(L + M), \text{ and} \tag{42}$$

$$Z_{DM} = j\omega(L - M). \tag{43}$$

Equation (42) is based on the equality among I_1, I_2, and I_C for common-mode circuits. Equation (43) is based on the equality among I_D, I_1, and $-I_2$, for differential-mode circuits.

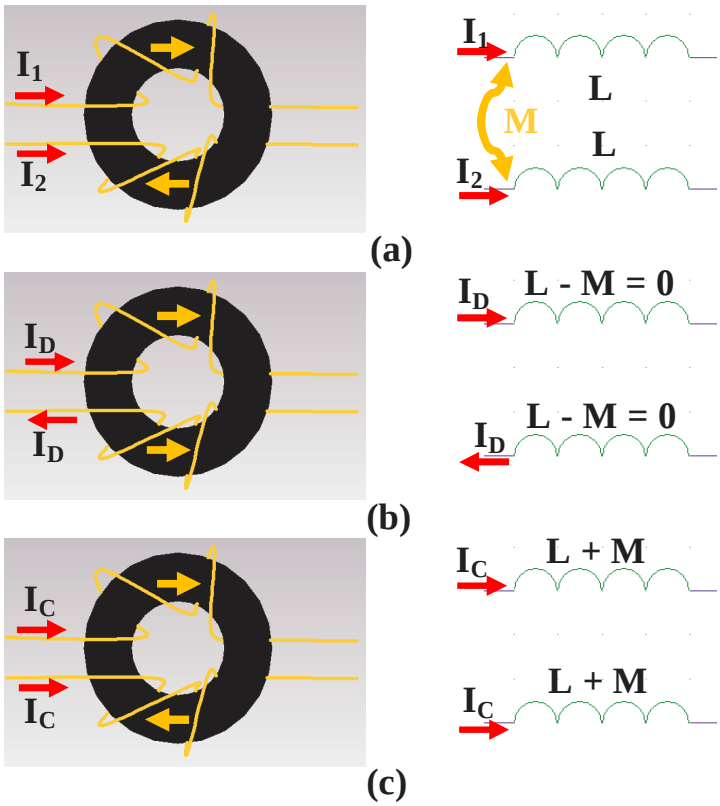

Figure A.3. Modeling the effect of common-mode and differential-mode currents.

If the windings are symmetric and flux remains in the core, there is no differential mode impedance because L is equal to M in an ideal case. In this case, the common-mode choke has no effect on differential-mode currents, but it increases the common-mode impedance ($Z_{cm} = j2\omega L$) so that common-mode currents are drastically reduced.

BIBLIOGRAPHY

[1] Andrey N. Lagarkov, Konstantin N. Rozanov, "High-frequency behavior of magnetic composites," Journal of Magnetism and Magnetic Materials 321 (2009), pp. 2082–2092.

[2] Clayton R. Paul. *Introduction to Electromagnetic compatibility*, Ch. 5, 10, John Wiley & Sons Inc, 2nd edition, 2006.

[3] S. Wakamatsu, F. Tilley, G. Hubers, Y. Sakamoto, T. Kaneko, H. Yamamoto and Y. Kurokawa "To reinforce immunities around GHz frequencies by EMI-noise suppression filters," pp. 511-514, *IEEE International Symposium on Electromagnetic Compatibility*, Aug. 1996.

[4] M. Hulkkonen, T. Veijola, A. Kallio, M. Andersson, M. Valtonen, "Measurement-Based Equivalent Circuit Model for Ferrite Beads," pp. 363-366, *European Conference*, Aug. 2009.

[5] Perambur S. Neelakanta. *Handbook of Electromagnetic materials. Monolithic and Composite Versions and Their Applications*, Ch. 14, 15, 21, CRC Press LLC, 1995.

[6] Jianfeng Xu, M. Y. Koledintseva, Yongxue He, R. E. DuBroff, J. L. Drewniak, B. Matlin, A. Orlando, "Measurement of Electromagnetic Parameters and FDTD Modeling of Ferrite Cores," pp. 83-88, *IEEE International Symposium*, August 2009.

[7] J. Zhang, M. Y. Koledintseva, and J. L. Drewniak, "Reconstruction of dispersive dielectric properties for PCB substrates using a genetic algorithm," *IEEE Trans. Electromag. Compat.*, vol. 50, no. 3, pp. 704-714, Aug. 2008.

[8] M. Koledintseva, J. Drewniak, Y. Zhang, J. Lenn, and M. Thoms, "Engineering of ferrite-based composite materials for shielding enclosures," J. Magnetism Magn. Mater. (JMMM), vol. 321, pp. 730-733, March 2009.

[9] D. M. Pozar, *Microwave engineering*, Ch. 3, 4, John Wiley & Sons Inc, – 3rd edition, 2005.

[10] O. Fujiwara, T. Ichikawa, “An Analysis of Load Effect Produced by Feerite Core Attachment,” Electronics and Communications in Japan, Part 1, Vol. 80, No. 9, 1997.

[11] Li, J. Neubel, J. L. Drewniak, R. E. DuBroff, T. H. Hubing and T. P. Van Doren, “EMI from airflow aperture arrays in shielding enclosures – experiments, FDTD and MOM modeling,” *IEEE transactions on Electromagnetic compatibility*, Vol. 42, No. 3, August 2000.

[12] M. Y. Koledintseva, P. C. Ravva, R. E. DuBroff, J. L. Drewniak, K. N. Rozanov, and B. Archambeault, “Engineering of Composite Media for Shields at Microwave Frequencies,” Proc. IEEE Symp. Electromag. Compat., August 2005, Chicago, IL, vol. 1, pp. 169-174.

[13] M. Y. Koledintseva, V. V. Bodrov, I. V. Sourkova, M. M. Sabirov, and V. I. Sourkov, “Unified spectral technique application for study of radiator behavior near planar layered composites,” *Progress in Electromagnetic Research (PIER)*, vol. 66, pp. 317-357, 2006.

VITA

Andrea Orlando was born in Atri (TE), Italy, on April 27, 1983. He received his Laurea degree (104/110) and his Specialistic degree (106/110) in Electric Engineering from the University of L'Aquila, L'Aquila, Italy, in 2005 and 2007, respectively. He was involved in the research activities of the UAq EMC Laboratory from July 2006 to December 2007. From June 2006 to June 2007, he had an internship at Selex Communications s.p.a., working with the layout/SI/PI design group. In January 2008 he joined the EMC Laboratory at the Missouri University of Science and Technology, where he received his Master of Science Degree in Electrical Engineering in December 2009. His main research interests are in the field of EMC/EMI, and in particular in shielding materials and common-mode suppressors.